

The 617 MHz - λ 850 μm Correlation (Cosmic Rays and Cold Dust) in NGC 3044 and NGC 4157

J. A. Irwin^{1*}, R. S. Brar², D. J. Saikia³ and R. N. Henriksen¹

¹*Dept. of Physics, Engineering Physics, & Astronomy, Queen's University, Kingston, Ontario, Canada, K7L 3N6*

²*Faculty of Science, University of Ontario Institute of Technology, 2000 Simcoe Street North, Oshawa, Ontario, Canada L1H 7K4*

³*National Centre for Radio Astrophysics, TIFR, Pune University Campus, Post Bag 3, Pune, 411 007, India; Cotton College State University, Panbazar, Guwahati, 781 001, India*

Accepted.... Received ...

ABSTRACT

We present the first maps of NGC 3044 and NGC 4157 at λ 450 μm and λ 850 μm from the JCMT as well as the first maps at 617 MHz from the GMRT. High latitude emission has been detected in both the radio continuum and sub-mm for NGC 3044 and in the radio continuum for NGC 4157, including several new features. For NGC 3044, in addition, we find 617 MHz emission extending to the north of the major axis, beginning at the far ends of the major axis. One of these low intensity features, more than 10 kpc from the major axis, has apparently associated emission at λ 20 cm and may be a result of in-disk activity related to star formation.

The dust spectrum at long wavelengths required fitting with a two-temperature model for both galaxies, implying the presence of cold dust ($T_c = 9.5$ K for NGC 3044 and $T_c = 15.3$ K for NGC 4157). Dust masses are $M_d = 1.6 \times 10^8 M_\odot$ and $M_d = 2.1 \times 10^7 M_\odot$ for NGC 3044 and NGC 4157, respectively, and are dominated by the cold component.

There is a clear correlation between the 617 MHz and λ 850 μm emission in the two galaxies. In the case of NGC 3044 for which the λ 850 μm data are strongly dominated by cold dust, this implies a relation between the non-thermal synchrotron emission and cold dust. The 617 MHz component represents an integration of massive star formation over the past 10^{7-8} yr and the λ 850 μm emission represents heating from the diffuse interstellar radiation field (ISRF).

The 617 MHz - λ 850 μm correlation improves when a smoothing kernel is applied to the λ 850 μm data to account for differences between the CR electron diffusion scale and the mean free path of an ISRF photon to dust. The best-fit relation is $L_{617\text{MHz}} \propto L_{850\ \mu\text{m}}^{2.1 \pm 0.2}$ for NGC 3044. If variations in the cold dust emissivity are dominated by variations in dust density, and the synchrotron emission depends on magnetic field strength (a function of gas density) as well as CR electron generation (a function of massive star formation rate and therefore density via the Schmidt law) then the expected correlation for NGC 3044 is $L_{617\text{MHz}} \propto L_{850\ \mu\text{m}}^{2.2}$, in agreement with the observed correlation.

Key words: galaxies: individual: NGC 3044, NGC 4157; galaxies: ISM; infrared: galaxies; radio continuum: galaxies

1 INTRODUCTION

1.1 Cosmic Rays and Dust in Disk-Halo Outflows

Observations of edge-on, star-forming galaxies indicate that many (possibly most) such systems display extra-planar

emission ('halos'). Where sufficient observations exist, these halos are known to be both multi-phase, displaying all of the components of the in-disk interstellar medium (ISM), as well as highly structured, revealing vertical features over a variety of spatial scales (e.g. Lee et al. 2001). Mass flux estimates thus far (Bregman & Pildis 1994; Wang et al. 1995, 2001; Fraternali et al. 2002) imply that disk-halo outflow is responsible for transporting large quantities of gas and, as a result, has an important role to play in the evolution of

* E-mail: irwin@astro.queensu.ca (JAI); Rupinder.Brar@uoit.ca (RSB); djs@ncra.tifr.res.in (DJS); henriksn@astro.queensu.ca (RNH)

galaxies, from metallicity gradients in disks to altered star formation rates (SFRs). Spatially resolved observations of nearby edge-on galaxies provide us with important data for studying the details of such disk-halo outflows.

Early observations of edge-on galaxies showed that radio continuum emission can extend several kpc above the plane (Hummel & van der Hulst 1989; Hummel, Beck, & Dettmar 1991), and this emission is dominated by non-thermal synchrotron radiation (e.g. Irwin, English & Sorathia 1999; Irwin, Saikia & English 2000), indicative of magnetic fields and cosmic rays (CRs). Galactic winds may also be present, since CRs can drive outflows, as first pointed out by Ipavich (1975); such outflows or ‘feedback’ are crucial to galaxy formation scenarios.

Dust in galaxy halos was first observed in the form of vertical filaments in absorption against starlight (Sofue 1987) and, later in emission from high resolution space-based infra-red (IR) observations (e.g. Irwin & Madden 2006). Extracting the physical conditions of dust, which is present over a range of sizes, compositions and excitation conditions, requires careful modelling of the spectral energy distribution (SED) and therefore observations at a variety of infrared wavelengths. Although such modelling is routinely carried out for galaxy disks, it has proved more difficult for the weaker halo emission [but see Whaley et al. (2009)]. With fewer data points, however, it is still possible to constrain some dust properties (e.g. Dunne et al. 2000; Dunne & Eales 2001), especially in the ‘classical’ regime in which grains reach equilibrium temperatures.

In this paper, we present the results of observations at 617 MHz as well as at two sub-mm wavelengths, λ 450 μ m and λ 850 μ m, of two edge-on galaxies – NGC 3044 and NGC 4157 – in order to study both the in-disk emission and any halo emission which might be present. Since synchrotron emission is stronger at lower frequencies, halos should be more easily detected than at high radio frequencies for comparable signal-to-noise (S/N). A clear example can be found in Irwin & Saikia (2003). As for dust, the sub-mm wavelengths are known to be probes of cold dust and are less likely to be contaminated by contributions from hot or warm components and/or stochastically heated very small grains. Such data also provide the best estimate of total dust mass. Adopting these wavebands also allows us to probe the far infrared (FIR) - radio continuum relation (see next subsection) in these galaxies.

In the next two subsections, we discuss the FIR - radio continuum relation and introduce the two galaxies. In Sect. 2, we provide details of the observations and data reduction. Sect. 3 presents the results, including high latitude emission, where present, temperature fitting, mass estimates, and sub-mm-radio correlations. Sects. 4 and 5 present the discussion and conclusions, respectively.

1.2 The FIR-Radio Continuum Relation

The well-known relationship between thermal FIR emission from dust and the predominantly non-thermal synchrotron emission in galaxies (de Jong et al. 1985; Helou et al. 1985) is believed to result from the dependence of both on massive star formation (Wunderlich & Klein 1988). The same stars that provide ultraviolet (UV) photons to heat the dust are also destined to become supernovae, thus producing non-

thermal radio emission. What is still a puzzle, however, is how the relation can be so tight over many orders of magnitude among galaxies that have a range of properties, for example, differing ISM masses, dust masses, metallicities, SFRs and possible differences as to how optically thick or optically thin galaxies are to UV photons and CR electrons. Similar arguments apply to the correlation which has also been found *within* galaxies. As a result, other possibilities have been proposed for the origin of the relation, for example coupling between the magnetic field strength and the gas density; since it is well known that gas and dust density vary together, one would expect higher synchrotron emission wherever the dust emission is higher (Helou & Bicay 1993; Hoernes et al. 1998; Groves et al. 2003).

One observational difficulty has been the traditional choice of the 1.4 GHz radio frequency (which includes a small but non-negligible thermal contribution) and FIR emission at λ 60 and λ 100 μ m (which includes contributions from both warm and cold dust). An early attempt at separating the various spectral contributions within M 31 (Hoernes et al. 1998) suggested that a good relation still exists between non-thermal radio emission and *cold* dust, the former driven by supernovae and the latter heated by the general interstellar radiation field (ISRF) rather than solely by hot young stars, i.e. the direct link with star-forming regions is less clear. Pierini et al. (2003) later found a slightly non-linear relation between the radio continuum and cold dust ($L_{1.4\text{GHz}} \propto L_{\text{cold dust}}^{1.13}$) and suggest that there may be a non-linear dependence of radio emission on SFR. See also Tabatabaei et al. (2010a) and Tabatabaei et al. (2010b) for further discussion.

A better approach is to observe the radio emission at a frequency that is strongly dominated by the non-thermal component, so that assumptions and corrections for the thermal contribution are not required. This is especially important when searching for correlations within a given galaxy since the thermal contribution can vary strongly from place to place. We have taken this approach by choosing the low radio frequency of 617 MHz. Similarly, by searching for correlations with λ 850 μ m emission, the ISRF-heated cold dust component is more likely to be isolated. Such an approach has been taken by Brar, Irwin & Saikia (2003) who find a good correlation between these two wavebands within the galaxy, NGC 5775.

An important refinement is to consider whether a smoothed version of the sub-mm emission improves upon the relation, should one be found. For example, Bicay & Helou (1990) proposed that, since the mean free path of a UV photon to dust absorption is much less than the diffusion length of a typical CR electron, we would expect that the FIR-radio continuum relation (or, in our case, the 617 MHz - 850 μ m relation) will be improved if the FIR emission is smoothed spatially. Such an improvement has been observed by Murphy et al. (2006a, 2006b, 2008, 2009). We will examine this refinement for NGC 3044 and NGC 4157 as well.

1.3 The galaxies

Optical images of NGC 3044 and NGC 4157 are shown in Fig. 1 and their basic parameters are listed in Table 1. Aside from the fact that NGC 4157 resides in a richer environment

colour_fig.jpg

Figure 1. Colour images of NGC 3044 (left) and NGC 4157 (right) from the Sloan Digital Sky Survey (SDSS). *This figure is included as a jpeg file accompanying this manuscript.*

(see below), the two galaxies have similar global properties: to within a factor of about 1.5, the galaxies are of similar size, SFR, total mass, and gas content. One difference is in the colour of the emission as seen in Fig. 1 and indicated by the $(B-V)_T$ colour of Table 1. NGC 3044 shows predominantly blue emission throughout its projected disk, whereas NGC 4157 shows blue emission in the outer regions. There is a small difference in inclination between the two galaxies which may contribute to this colour difference though it isn't clear to what extent. For example, the slightly lower inclination of NGC 4157 appears to allow the redder inner regions of the galaxy to be more readily revealed. We describe these galaxies in detail, below.

1.3.1 NGC 3044

NGC 3044 (Fig. 1 left) is an isolated galaxy with no known companions. Although Tully (1988) place it within the Leo Cloud, the other 3 members are widely displaced in the sky ($> 6^\circ$ or > 2.3 Mpc). Some minor warping can be seen in the optical image at large galactocentric radii, however, and asymmetries between the north-west and south-east major axis emission have been noted by Lee & Irwin (1997) and Collins et al. (2000). NGC 3044 has been considered both a 'starburst' and 'normal' galaxy; Tüllmann et al. (2006) discuss this issue, indicating that it may be considered a starburst galaxy, but one in which the starburst is extended over most of the disk, rather than concentrated near the nucleus.

The presence of a galactic halo in NGC 3044 is well known, having first been discovered in the radio continuum by Hummel & van der Hulst (1989) and further observed by various authors (e.g. Condon et al. 1990; Colbert et al. 1996; Irwin, English & Sorathia 1999; Irwin, Saikia & English 2000). Extra-planar diffuse ionized gas (eDIG) has been detected by Collins et al. (2000), Tüllmann & Dettmar (2000) and Miller & Veilleux (2003) and extends as far as 5 kpc from the plane (Tüllmann et al. 2006)¹. Halo structure, including a kpc-scale diameter H α arc on the south side of the disk is also observed (Miller & Veilleux 2003). Ionization of the eDIG can be explained by a combination of photo-ionization and shock ionization (Tüllmann & Dettmar 2000). XMM-Newton observations by Tüllmann et al. (2006) have detected an extended soft X-ray halo which reaches its maximum height over the inner disk ($R < 6$ kpc). The X-ray emission correlates with both the eDIG and radio continuum. Halo HI emission is also observed, including HI exten-

sions and several loops that have the signature of expanding supershells (Lee & Irwin 1997). There appears to be some spatial correlation between the HI and radio continuum features in the inner disk, but the HI is more extended radially and shows vertical extensions that do not have counterparts at other wavebands. Infrared spectroscopy of the halo has also been recently obtained by Rand et al. (2011).

A supernova was observed in NGC 3044 in the year, 1983².

1.3.2 NGC 4157

NGC 4157 (Fig. 1 right) is a member of the Ursa Major Cloud (Tully 1988) and belongs to the galaxy group, LGG-258 (Garcia 1993). Previous radio continuum observations have been made by Condon (1987), Gioia & Fabbiano (1987), Hummel & van der Hulst (1989), Irwin, English & Sorathia (1999) and Irwin, Saikia & English (2000). HI data can be found in Rhee & van Albada (1996), in Verheijen & Sancisi (2001), in the Westerbork HI survey of Spiral and Irregular Galaxies (WHISP) catalog³ (see e.g. Noordermeer et al. 2005), and in Kennedy (2009). A companion galaxy, UGC 7176, with a dynamical mass $\approx 1\%$ of that of NGC 4157, is located 12 arcmin to the south (Kennedy 2009). CO parameters can be found in Young et al. (1995) and Komugi et al. (2008). The galaxy was observed with the Infrared Space Observatory (ISO) at λ 12 μ m (Bendo et al. 2002) and a UV image from the Galaxy Evolution Explorer (GALEX) satellite can be found in Gil de Paz et al. (2007).

A radio continuum halo was discovered in NGC 4157 by Irwin et al. (1999) but, to our knowledge, the only previous search for extraplanar features in this galaxy was made by Howk & Savage (1999) who searched for extraplanar dust absorption, with ambiguous results.

Three historical supernovae have been detected in NGC 4157 in the years, 1937, 1955 and 2003 (see Footnote 2).

2 OBSERVATIONS & DATA REDUCTION

2.1 Radio Continuum Data

Observations of NGC 3044 and NGC 4157 were obtained with the Giant Metrewave Radio Telescope (GMRT), lo-

¹ Adjusted to our distance and so throughout.

² Data from the International Astronomical Union Central Bureau for Astronomical Telegrams at <http://www.cfa.harvard.edu/iau/lists/Supernovae.html>.

³ see <http://www.astro.rug.nl/~whisp/>

Table 1. Galaxy Parameters

Parameter ^a	NGC 3044	NGC 4157
Morphological Type	SB(s)c? sp (HII)	SAB(s)b? sp (HII)
RA (J2000) (h m s)	9 53 40.9	12 11 04.4
DEC (J2000) (° ' ")	1 34 47	50 29 05
Distance, d (Mpc) ^b	21.7 ^c	12.9 ^d
Optical major \times minor axis (' \times ')	5.71 \times 0.63	7.95 \times 1.06
D_{25} (' , kpc) ^e	4.90, 30.9	6.76, 25.4
Inclination (°)	85 ^c	83 ^f
Position angle (°)	113 ^c	66 ^d
Blue Magnitude	12.46	12.15
(B-V) _T ^g	0.53 \pm 0.02	0.80 \pm 0.01
$S_{12}, S_{25}, S_{60}, S_{100}$ (Jy) ^h	0.60, 1.11 9.64, 19.38	1.72, 2.12, 17.71, 50.67
$\sigma_{12}, \sigma_{25}, \sigma_{60}, \sigma_{100}$ (mJy) ⁱ	22, 86 30, 89	39, 28, 43, 170
S_{60}/S_{100}	0.497	0.350
F_{FIR}, F_{IR} (10^{-9} erg s ⁻¹ cm ⁻²) ^j	0.558, 1.05	1.21, 2.35
L_{FIR}, L_{IR} ($10^{10} L_{\odot}$) ^k	0.820, 1.55	0.631, 1.22
$L_{FIR}/D_{25}^2, L_{IR}/D_{25}^2$ (10^{40} erg s ⁻¹ kpc ⁻²)	3.29, 6.21	3.76, 7.26
SFR (M_{\odot} yr ⁻¹) ^l	2.7	2.1
M_{HI} ($10^9 M_{\odot}$) ^m	5.4 \pm 0.4	4.2 \pm 0.1
M_{H_2} ($10^9 M_{\odot}$) ⁿ	2.1 \pm 50%	1.8 \pm 30%
M_{dyn} ($10^{11} M_{\odot}$) ^o	1.5 \pm 0.2	2.0 \pm 0.5

^a Values from the NASA/IPAC Extragalactic Database (NED) unless otherwise indicated.

^b The quoted values agree, within errors, with NED Hubble Flow distances with respect to the Cosmic Microwave Background for $H_0 = 73$ km s⁻¹ Mpc⁻¹.

^c Lee & Irwin (1997).

^d Irwin, English & Sorathia (1999).

^e Optical diameter at the 25th magnitude isophote, from de Vaucouleurs et al. (1991).

^f Tully et al. (1996).

^g Total B-V colour from de Vaucouleurs et al. (1991).

^h IRAS flux densities at λ 12 μ m, λ 25 μ m, λ 60 μ m and λ 100 μ m, respectively, from Sanders et al. (2003).

ⁱ Errors on IRAS flux densities of previous row.

^j FIR (λ 40 \rightarrow 500 μ m) and IR (λ 8 \rightarrow 1000 μ m) flux density, respectively, according to the prescription of Sanders & Mirabel (1996), with their constant, $C = 1$.

^k FIR and IR luminosity, respectively, from $L = 4\pi d^2 F$, with $L_{\odot} = 3.83 \times 10^{33}$ erg s⁻¹.

^l Star formation rate, from L_{IR} , according to the prescription of Kennicutt (1998).

^m HI mass (Lee & Irwin 1997 for NGC 3044; Kennedy 2009 for NGC 4157).

ⁿ H_2 mass using a conversion factor of $X = 2.0 \times 10^{20}$ mol cm⁻² (K km s⁻¹)⁻¹ (Solomon & Sage 1988 for NGC 3044; Young et al. 1996 for NGC 4157).

^o Total dynamical mass from HI data (Lee & Irwin 1997 for NGC 3044; Kennedy 2009 for NGC 4157).

Table 2. GMRT Observations

	NGC 3044	NGC 4157
Date of Observation	26 July 2002	27 July 2002
On-source Observing Time (min.)	404	280
Primary Flux Density Calibrator	3C 286	3C 286
Phase Calibrator	J0943-083	J1146+399
No. of Spectral Channels	128	128
Channel Width (kHz)	125	125
Central Frequency (MHz) ^a	617.375	619.937
Total Bandwidth (MHz) ^a	9.875	9.375
Primary Beam FWHM (arcmin)	47.4	47.2

^a After editing

cated near Pune, India, which consists of 30 antennas, each 45 m in diameter, in a fixed, ‘Y’-shaped array with a longest baseline of about 25 km and the shortest, 100 m. Fourteen of the antennas are clustered randomly in a central 1×1 km central ‘square’ with the remainder in the arms. At the time of the observations, not all antennas were available, leaving typically, 25 to 29 antennas for each observation. For a more complete description of the telescope, see Swarup (1991), Swarup et al. (1991), Ananthkrishnan (2005) or <http://www.gmrt.ncra.tifr.res.in>. A summary of the observational data is given in Table 2. Note that the shortest spacing ensures that, at 617 MHz, spatial scales up to about 17 arcmin are detected, i.e. about 3 times and 2 times the optical major axis diameters of NGC 3044 and NGC 4157, respectively.

Observations were carried out in the standard fashion, with a flux density calibrator observed during the observing run and phase calibrators observed at regular intervals, typically every 30 minutes. The spectral line mode, which is the default at the GMRT, was used to identify interference, if present. The data were processed using the Astronomical Image Processing System (AIPS) of the National Radio Astronomy Observatory (NRAO). Editing was initially carried out using the AIPS-compatible routine, GMRED⁴ which we wrote in order to remove bad data, since the GMRT did not have on-line flagging during the observations. Further editing was then carried out in AIPS using standard routines. After editing, the central frequencies were slightly different for the two galaxies (Table 2), but we will refer to both data sets as the 617 MHz data.

Standard continuum calibration was carried out except for the additional step of bandpass calibration using the phase calibrators. The uv data were then Fourier-transformed, the dirty beam deconvolved and the clean beam reconvolved using the AIPS routine, IMAGR. This required forming a number of fields so that significant sources far from the field center could be properly imaged and cleaned. Maps were originally formed for every channel so that each one could be checked for consistency. This led to some further editing and re-calibration. The uv data in the remaining channels were then averaged to form a single-channel data set. From these data, maps were formed using a range of uv weightings resulting in a range of spatial resolutions and signal-to-noise (S/N) ratios, from which we present the 9 arcsec and 15 arcsec resolution images in Figs. 2a and b and Figs. 4a and b. The undisplayed images do not reveal any features that are not seen on these two.

The final step was to correct for the primary beam of the GMRT. This correction, however, introduces position-dependent noise over the image and, since the total flux correction was measured to be less than 0.4% for both galaxies after the primary beam correction (much less than other errors), we adopt the uncorrected maps for presentation and further analysis.

We carried out observations of NGC 3044 and NGC 4157 at 327 MHz also. However, the resulting data sets were not of sufficient quality to use. Since we have previously obtained Very Large Array (VLA) data of NGC 3044

and NGC 4157 at λ 20 cm, these data are also presented here (Figs. 3 and 5, respectively) to supplement our GMRT data. For details on these data sets, see Irwin, English & Sorathia (1999).

2.2 Sub-mm Images

Sub-mm observations of NGC 3044 and NGC 4157 were obtained with the Submillimetre Common-User Bolometer Array (SCUBA, see Holland et al. (1999)) on the James Clerk Maxwell Telescope (JCMT⁵). The λ 450 μ m and λ 850 μ m arrays, which were used concurrently, consist of 91 and 37 circular pixels, respectively. The configuration of the pixels gives an instantaneous field of view of $2.3'$. Observations were carried out in 64-point jiggle-map mode which ensures Nyquist sampling at both frequencies. Hourly pointing checks were made during the observations and measurements to determine the atmospheric transparency were also carried out. Two fields of view were required to cover each galaxy. The final field of view and other observing data are given in Table 3. We will refer to these data as the λ 450 μ m and λ 850 μ m data.

The data were reduced using the SCUBA User Reduction Facility (SURF) package (Jenness & Lightfoot 1999). The steps included regridding to true sky positions, atmospheric subtraction, flatfielding, and correction for sky opacity. For the latter, the optical depth from the Caltech Sub-mm Observatory, τ_{CSO} , was used, extrapolated to the observing wavelengths, and interpolated in time. Since there are not many pixels with no galaxy emission, sky values were calculated by first removing source emission from the data prior to sky subtraction⁶. The data were also examined carefully and edited for noisy bolometers and data spikes. Corrections for positional drift were applied and the data were calibrated using values of the known flux density calibrators for the times of observation. At this point, the data consisted of a sequence of calibrated images in time. Each image was then re-checked for bad data and additional flagging was carried out if the pixel value deviated by more than 5σ from the mean pixel value from all images. The final image was then made from an average of all images, weighted by integration time and background noise. The final step involved blanking the periphery of the final field of view (which contains two $2.3'$ fields) where the noise was higher than the average over the general field.

Since these data were obtained, di Francesco et al. (2008) have independently reduced the same data set with good agreement in the results. We will compare our results to theirs, where relevant, in subsequent sections.

Finally, we consider the possibility of contamination of the λ 850 μ m band by CO(J=3-2) emission. For NGC 3044, this can be tested explicitly since we have CO(J=3-2) data from Lee (1998) who find a maximum brightness temperature of 0.091 K with an effective line width of 89 km s^{-1} (width of $\Delta\lambda = 7.5 \mu\text{m}$) within a 14.9 arcsec beam at a

⁴ This AIPS-compatible routine was written by us and is available at <http://www.astro.queensu.ca/~irwin>.

⁵ The JCMT is supported by the Science and Technology Facilities Council of the UK, the NRC of Canada, and the Netherlands Organization for Scientific Research.

⁶ The SURF routine, CALCSKY, was used.

location near the radio continuum peak. Our peak continuum flux density of $69.4 \text{ mJy beam}^{-1}$ in a 15 arcsec beam (Fig. 2d) corresponds to 2.1 K within the SCUBA $850 \mu\text{m}$ bandwidth of $70 \mu\text{m}$ (Holland et al. 1999). Therefore, the estimated contamination is less than 1%. It is well known that contamination of the SCUBA $450 \mu\text{m}$ band by CO(J=6-5) is even lower (e.g. Seaquist et al. 2004).

3 RESULTS

The final maps are shown in Fig. 2 for NGC 3044, and Fig. 4 for NGC 4157. Beam sizes and noise value information can be found in the figure captions. We discuss the results for the two galaxies, separately.

3.1 The NGC 3044 Maps

3.1.1 Radio Continuum Images

Figs. 2a and b show 617 MHz data for NGC 3044, illustrating both the in-disk as well as high latitude radio continuum emission of this galaxy, and the flux density is given in Table 4. The data have been shown with two different uv weightings to illustrate the fine structure emission (Fig. 2a) as well as larger scale structure at higher sensitivity (Fig. 2b). At 617 MHz, the emission is strongly dominated, unambiguously, by non-thermal synchrotron radiation. For comparison, we show the $\lambda 6 \text{ cm}$ and $\lambda 20 \text{ cm}$ VLA maps from Irwin, English & Sorathia (1999) in Fig. 3 over the same field of view as Fig. 2. As shown by Irwin, English & Sorathia (1999), the $\lambda 6 \text{ cm}$ and $\lambda 20 \text{ cm}$ maps are also dominated by non-thermal emission. In addition, we compute the global spectral index between the 617 MHz and $\lambda 20 \text{ cm}$ emission to be $\alpha = -0.72 \pm 0.25$; this spectral index strongly departs from what would be expected for thermal emission ($\alpha_{\text{thermal}} = -0.1$).

The 617 MHz radio continuum emission in the disk of NGC 3044 is highly asymmetric, being extended on the north-west side but has a more ‘truncated’ appearance on the south-east side. Asymmetries, in just this sense, can be seen in the X-ray image (Tüllmann et al. 2006) and in H α (e.g. Collins et al. 2000) as well as the $\lambda 6 \text{ cm}$ and $\lambda 20 \text{ cm}$ maps. As has been pointed out earlier (Sect. 1), the X-ray, radio continuum, and H α all appear correlated. The asymmetry observed in HI, however, does not correlate in the same sense. The HI distribution is extended more on the south-east disk than in the north-west (Lee & Irwin 1997).

The extraplanar radio continuum emission is highly structured, as has been seen before in radio halos of other edge-on galaxies (e.g. Lee et al. 2001) though the halo is not as pronounced as in the VLA maps likely because the VLA observations have somewhat higher dynamic range (255/1 and 362/1 for $\lambda 6 \text{ cm}$ and $\lambda 20 \text{ cm}$, respectively) than the 617 MHz observations (228/1). The uv distribution will also differ. The broadest halo can be seen on either side of the nuclear region, consistent with what is seen in H α and soft X-rays.

A new and interesting result is the appearance of the two far ends of the major axis, both of which show emission extending out of the plane towards the north and both of which show a ‘double-pronged’ appearance. That is, there is

Table 4. Measured and Derived Galaxy Properties

Property	NGC 3044	NGC 4157
$S_{617 \text{ MHz}}$ (Jy) ^a	0.20 ± 0.04	0.43 ± 0.05
$S_{450 \mu\text{m}}$ (Jy) ^b	3 ± 1	10 ± 2
$S_{850 \mu\text{m}}$ (Jy) ^b	0.75 ± 0.10	0.8 ± 0.1
T_c (K) ^c	9.5 ± 1.5	15.3 ± 3
T_w ^c (K)	31.0 ± 1.4	25.6 ± 0.9
N_c/N_w ^d	76	4
M_d ($10^8 M_\odot$) ^e	1.6 ± 0.6	0.21 ± 0.06
$M_{\text{gas}}/M_{\text{dust}}$ ^f	47	286

^a Flux density at 617 MHz. Uncertainties include variations in editing, and choice of imaging and self-calibration parameters over different reduction trials.

^b Flux density at 450 or 850 μm . Uncertainties include variations over different box sizes as well as variations between our data reduction and that of di Francesco et al. (2008).

^c Temperature of cold (subscript, c, and so throughout) or warm (subscript, w, and so throughout) dust component (see text).

^d Eqn. 2. The estimated error is $\approx 25\%$. This quantity is equivalent to M_c/M_w .

^e Eqn. 3.

^f From $M_{\text{HI}} + M_{\text{H}_2}$ of Table 1 and M_d from this table. The uncertainty could be as high as 90% for NGC 3044 and 60% for NGC 4157.

evidence for the ejection of cosmic rays away from the plane at both ends of the major axis; presumably, the ejection of particles is facilitated by the lower density ISM at these locations.

On the far south-east end of the major axis, moreover, where the radio continuum major axis emission is truncated, some disconnected emission features can be seen towards the north, including a large feature centered at RA $\approx 9^{\text{h}} 53^{\text{m}} 51^{\text{s}}$, DEC $\approx 01^\circ 35' 45''$ which we have labelled a ‘non-thermal cloud’ (NTC). The feature occurs at a low S/N, but the independent VLA $\lambda 20 \text{ cm}$ map and (to a lesser extent) in the VLA $\lambda 6 \text{ cm}$ map (Fig. 3) also show features in this direction. These features will be discussed further in Sect. 4.1.1.

3.1.2 Sub-mm Images

The sub-mm emission of NGC 3044 is shown in Fig. 2c and d. The field of view, delineated by the region over which contour emission is displayed, is much smaller than the radio continuum emission (see Table 3 for the field size). These maps show mainly the strong, in-disk emission, since the sensitivity is insufficient to delineate a global dust halo, if it exists. The $\lambda 850 \mu\text{m}$ map, however, does hint at a few discrete features; these will be discussed in Sect. 4.1.1.

The total $\lambda 450 \mu\text{m}$ and $\lambda 850 \mu\text{m}$ flux densities are given in Table 4. If emission at the level of the rms noise were to exist out to the ends of the optical major axis in the $\lambda 450 \mu\text{m}$ map (as is the case for the $\lambda 850 \mu\text{m}$ map), then the $\lambda 450 \mu\text{m}$ flux density would not change by more than the error bar that has been quoted. Therefore, the flux densities at the two frequencies can both be used to constrain dust properties, within the constraints of their uncertainties, as will be discussed in Sect. 3.3.

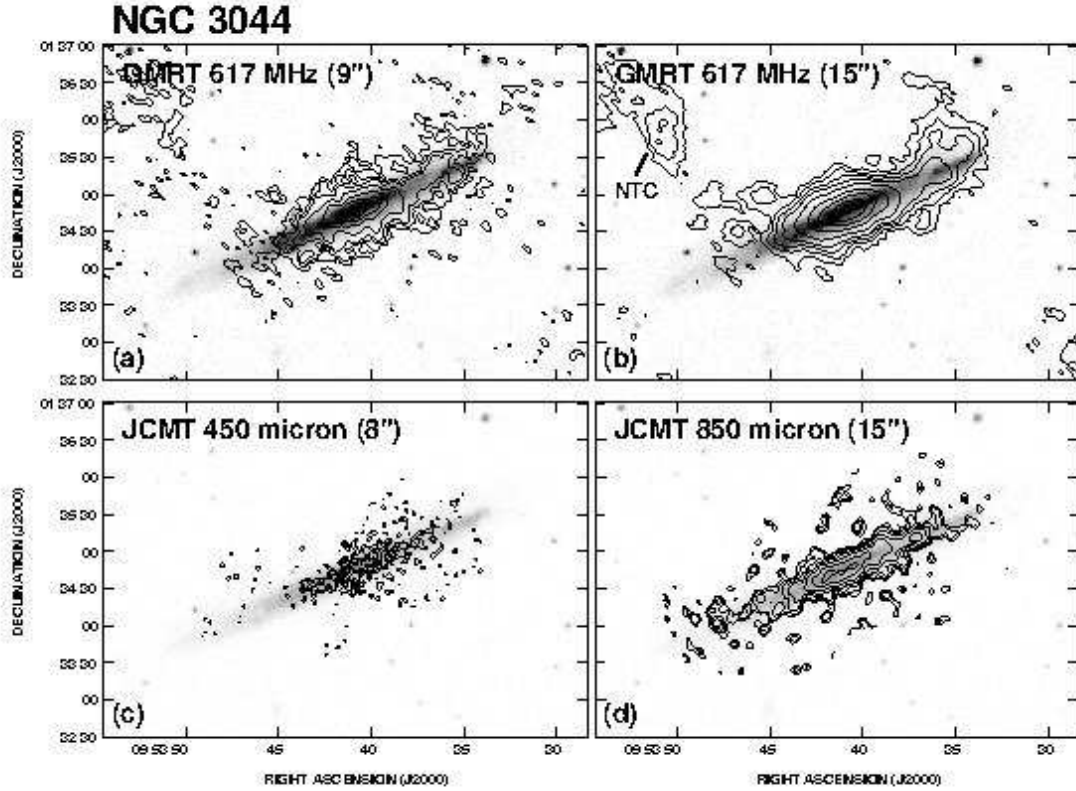


Figure 2. Radio continuum and sub-mm emission of NGC 3044 (contours) superimposed on a greyscale of the Digitized Sky Survey 2 (DSS2) blue image, whose grey range has been varied, as needed, to show the contours. In each case, the first contour has been set to 2σ , where σ is the rms noise of the image. (a) GMRT 617 MHz map with a resolution (circular beam FWHM and so throughout) of $9.0''$. Contours are at 0.29, 0.5, 0.75, 1.5, 3, 5, 7.5, and 10 mJy beam^{-1} and the map peak is $25.4 \text{ mJy beam}^{-1}$. (b) GMRT 617 MHz map (resolution = $15''$). Contours are at 0.24, 0.5, 0.9, 1.5, 3, 6, 10, 15, and 21 mJy beam^{-1} and the map peak is $27.4 \text{ mJy beam}^{-1}$. The non-thermal cloud (NTC) discussed in Sect. 4.1.1 is marked. (c) JCMT λ 450 μm map (resolution = $8.0''$). Contours are at 64, 100, 150, 200, and $300 \text{ mJy beam}^{-1}$ and the map peak is $307.8 \text{ mJy beam}^{-1}$. (d) JCMT λ 850 μm map (resolution = $14.9''$). Contours are at 9, 13, 18, 25, 35, 50 and 65 mJy beam^{-1} and the map peak is $69.4 \text{ mJy beam}^{-1}$.

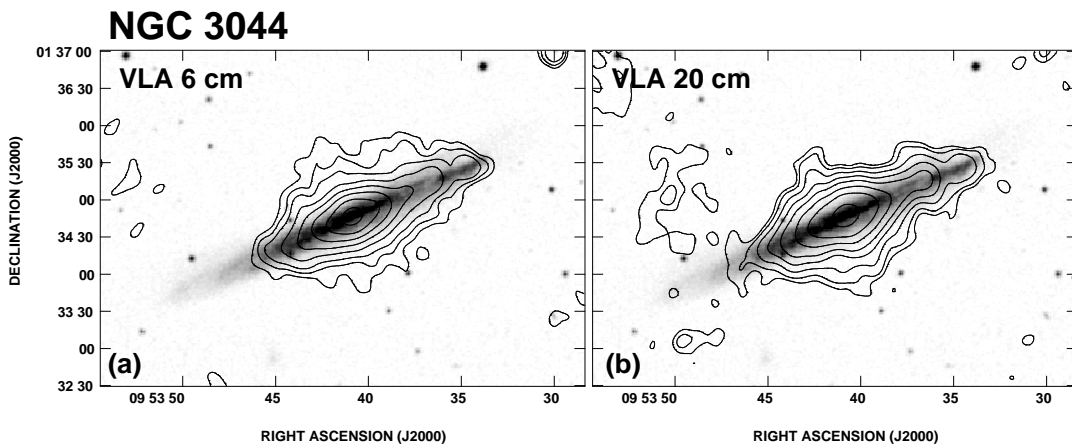


Figure 3. VLA radio continuum emission (contours) superimposed on the DSS2 blue image (greyscale). For more information, see Irwin et al. (1999). (a) λ 6 cm emission. The beam is $18.8'' \times 15.8''$ at a position angle of $\theta = 7.6^\circ$ and contours are at $0.08 (2\sigma)$, 0.15, 0.25, 0.5, 1, 2, 4, 8, and 10 mJy beam^{-1} . The map peak is $10.2 \text{ mJy beam}^{-1}$. (b) λ 20 cm emission. The beam is $18.9'' \times 15.9''$ at $\theta = -7.1^\circ$ and contours are at $0.12 (2\sigma)$, 0.2, 0.4, 0.8, 1.5, 3, 6, 15, and 21 mJy beam^{-1} . The map peak is $21.7 \text{ mJy beam}^{-1}$.

Table 3. JCMT Observations

	NGC 3044	NGC 4157
Dates of Observation	5, 6 Jan. 2001	12, 13 Jan. 2003
	15 Nov. 2001	11 Oct. 2003
On-source Observing Time (min.)	450	480
Flux Density Calibrators	Mars, CRL 618	Uranus, Mars
Central Wavelength (μm)	443, 863	443, 863
Resolution ($''$) ^a	8.0, 14.9	8.0, 14.4
Field of view (arcminute) ^{a b}	6.13, 8.0	6.48, 8.42

^a At $\lambda 450 \mu\text{m}$ and $\lambda 850 \mu\text{m}$, respectively.

^b After editing.

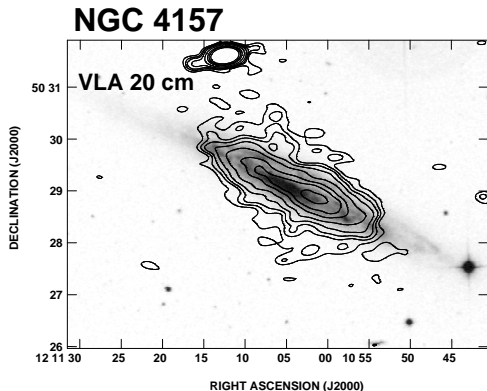


Figure 5. VLA radio continuum $\lambda 20$ cm emission (contours) superimposed on the DSS2 blue image (greyscale). For more information, see Irwin et al. (1999). The beam is $21.1'' \times 11.3''$ at $\theta = -81.4^\circ$ and contours are at 0.22 (2σ), 0.4 , 0.6 , 1 , 2 , 4 , 6 and 9 mJy beam^{-1} . The map peak is 44.1 mJy beam^{-1} .

3.2 The NGC 4157 Maps

3.2.1 Radio Continuum Images

The 617 MHz emission of NGC 4157 is shown in Fig. 4a and b and the flux density is given in Table 4. For comparison, the VLA $\lambda 20$ cm image is shown in Fig. 5 (a $\lambda 6$ cm image does not yet exist). The strongest radio emission belongs to a background point source that can be seen to the north of the galaxy on the far east side. The 617 MHz data agree very well with the VLA data throughout the disk. Fig. 4a and b appear to show a slight offset between the optical and radio major axes. However, this is because of a north-west/south-east asymmetry on either side of the major axis of the DSS2 blue image that has been displayed in the figure; the south-east side is the farther side and therefore the displayed optical blue emission is truncated by extinction on this side. The colour image of Fig. 1, for example, shows good north-west to south-east symmetry and the optical and radio major axes align well when comparing with the colour image.

The radio emission of the halo is also similar between the VLA $\lambda 20$ and 617 MHz emission, although the discrete extensions seen at $\lambda 20$ cm are less obvious at 617 MHz, possibly because of the lower dynamic range at 617 MHz (42/1

over the emission associated with NGC 4157 in Fig. 4b, compared to 93/1 for Fig. 5). The most obvious extension in Fig. 4b begins in the far north-eastern disk and extends approximately 1.5 arcmin (5.6 kpc) towards the south. It is visible at 617 MHz but not at $\lambda 20$ cm. If this feature is real, its spectral index must be less than $\alpha = -1.7$ ($I_\nu \propto \nu^\alpha$) to render it undetectable on the $\lambda 20$ cm image. No other independent detection of this feature has been made, but we note that it falls along the eastern side of an HI extension detected by Kennedy (2009); also spectral indices as low as $\alpha \approx -2$ have previously been detected in vertical features related to outflow in other galaxies (Heesen et al. 2011; Irwin et al. 2012). See Sect. 4.1.2 for further discussion.

3.2.2 Sub-mm Images

The $\lambda 450 \mu\text{m}$ and $\lambda 850 \mu\text{m}$ maps are shown in Figs. 4c and d, respectively, and flux densities are given in Table 4. Only in-disk emission can be seen in these full-resolution images. Again, there is the appearance of an offset in the major axis between the sub-mm emission and the optical emission. However, brightest optical emission aligns well with the brightest sub-mm emission, as shown in Figs. 4c and d to within the estimated pointing accuracy of 3 arcsec⁷, and, when the sub-mm emission maps are overlaid on the SDSS R-band image (not shown), the emission again centers squarely on the brightest optical emission. As we saw with the radio continuum emission, dust obscuration creates an apparent asymmetry in the optical images that have been displayed in the overlays.

The $\lambda 450 \mu\text{m}$ and $\lambda 850 \mu\text{m}$ emission in NGC 4157 extends approximately equally as far in radius; however, in both cases, neither is seen as far out as the optical disk. This is likely a sensitivity issue since the sub-mm dynamic range of the NGC 4157 data is lower than that of NGC 3044. This must be kept in mind when the two galaxies are compared.

⁷ We have also verified that the astrometry of the $\lambda 450 \mu\text{m}$ and $\lambda 850 \mu\text{m}$ maps agrees with the results of di Francesco et al. (2008) who have independently reduced the SCUBA data.

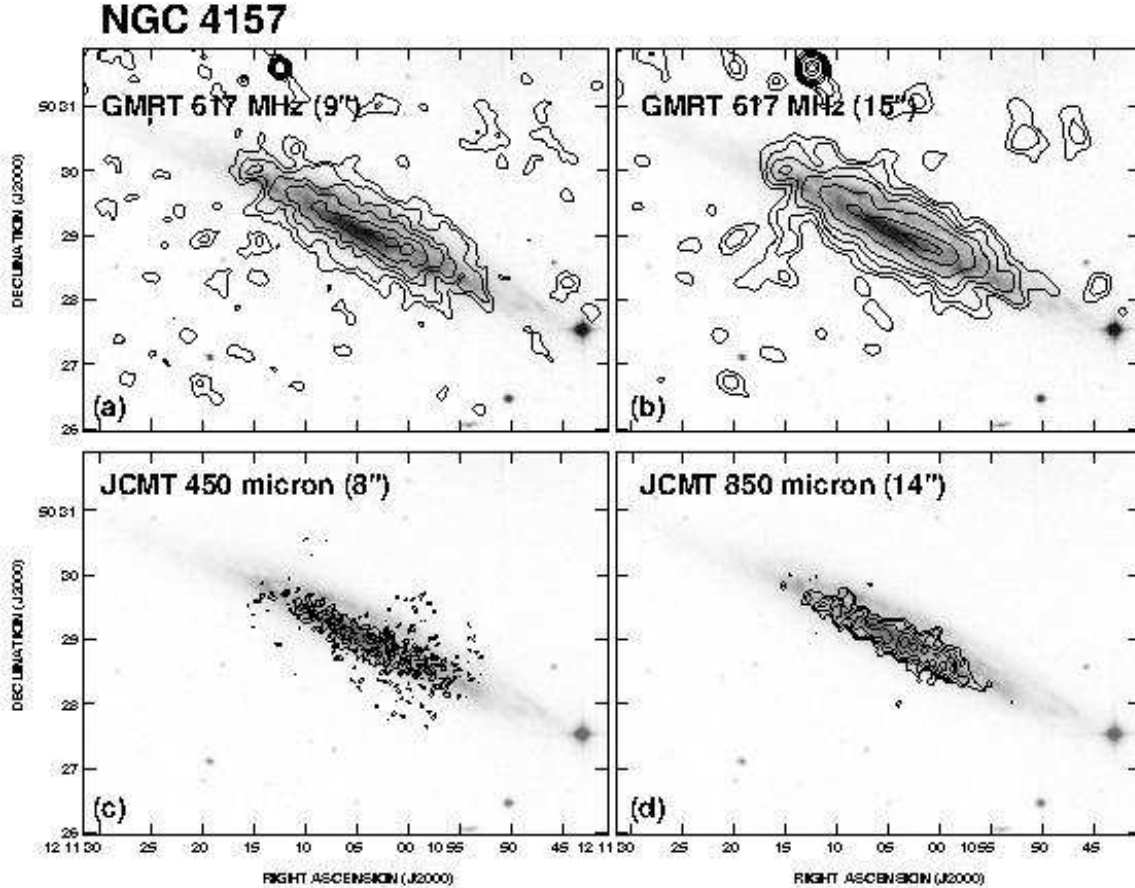


Figure 4. Radio continuum and sub-mm emission of NGC 4157 (contours) superimposed on a greyscale of the Digitized Sky Survey 2 (DSS2) blue image, whose grey range has been varied, as needed, to show the contours. In each case, the first contour has been set to 2σ , where σ is the rms noise of the image. (a) GMRT 617 MHz map with a resolution (circular beam FWHM and so throughout) of $9.0''$. Contours are at 0.68, 1.2, 2, 3, 5, and 7 mJy beam^{-1} and the map peak is $19.9 \text{ mJy beam}^{-1}$. (b) GMRT 617 MHz map (resolution = $15''$). Contours are at 0.88, 1.4, 2.3, 3.5, 6, 12, and 17 mJy beam^{-1} and the map peak is $20.0 \text{ mJy beam}^{-1}$. (c) JCMT λ 450 μm map (resolution = $8.0''$). Contours are at 102, 170, 250, and 350 mJy beam^{-1} and the map peak is $391 \text{ mJy beam}^{-1}$. (d) JCMT λ 850 μm map (resolution = $14.4''$). Contours are at 17, 25, 35, 45, and 55 mJy beam^{-1} and the map peak is $62.2 \text{ mJy beam}^{-1}$.

3.3 Dust Temperature, Mass and Gas/Dust Ratio

The IR/sub-mm spectra of NGC 3044 and NGC 4157, which include the IRAS flux densities (Table 1) as well as the sub-mm data (Table 4), are plotted in Fig. 6.

To determine the dust temperature, we consider only those ‘classical’ grains that are of sufficient size to reach an equilibrium temperature, rather than very small grains (VSGs) which are stochastically heated. Since the 12 and 25 μm flux densities are considered to be contaminated by VSGs (e.g. Dupac et al. 2003; Désert, Boulanger & Puget 1990) we exclude these points from our fits. For the remaining points, we assume that the dust is optically thin (see, e.g. Marengo et al. 1997; Eales & Edmunds 1996; Stevens & Gear 2000) and that the data can be described by a modified black body curve of the form

$$S_\nu = \Omega_d (\nu/\nu_0)^\beta B_\nu(T_d) \quad (1)$$

where S_ν is the flux density at frequency, ν , $B_\nu(T_d)$ is the Planck function for dust at temperature, T_d , Ω_d is the solid angle subtended by all dust (proportional to the number

of dust grains, N_d , in the optically thin limit), ν_0 is the frequency above which the dust becomes optically thick, and β is the emissivity index which we take to lie in the range, 1.5 to 2, as found from other studies of our own and other galaxies (e.g. Masi et al. 1995; Alton et al. 1998; Stevens & Gear 2000). The quantity, $(\nu/\nu_0)^\beta$ describes the optical depth. However, we could not fit the data, within errors bars, with a single-temperature model.

Although it is most realistic for the dust to have a spectrum of temperatures, we do not have sufficient data to test for such a spectrum. Instead, following Dunne & Eales (2001), James et al. (2002), Alton et al. (2000) and others, we fit a two-temperature (warm, denoted w, and cold, denoted c) model to the data. For identical dust grains that differ only by temperature, the spectrum is fit according to,

$$S_\nu = S_w + S_c = K \nu^\beta [N_w B_\nu(T_w) + N_c B_\nu(T_c)] \quad (2)$$

where N_w and N_c represent the number of warm and cold dust grains, respectively, S_w and S_c represent the flux density contributions of warm and cold dust grains, respectively, and K is a constant that folds in the solid angle subtended

by a dust grain and the frequency at which the dust becomes optically thick.

Since we have 4 useable data points per galaxy, we can solve only for the 4 parameters: KN_w , KN_c , T_w , and T_c . From these, we list the physically meaningful parameters, N_c/N_w , T_w , and T_c in Table 4 and show the fits in Fig. 6. The uncertainties on the temperatures are associated with the adopted range of β , i.e. $1.5 \leq \beta \leq 2.0$, which dominates over other uncertainties.

The temperatures given in Table 4 appear to be typical of what has been found by other authors who have applied two-temperature fits. For example, the ranges found by Dunne & Eales (2001) and James et al. (2002) for a large sample of galaxies were $28 \leq T_w$ (K) ≤ 60 and $17 \leq T_c$ (K) ≤ 32 . More recent data obtained from the Planck mission (Ade et al. 2011) find that, using two-temperature fits, a cold component ($T_c < 20$ K) is required in galaxies. Our results for both NGC 3044 and NGC 4157 are consistent with this. We also find that there is a greater range of dust temperature within NGC 3044 in comparison to NGC 4157. This appears to be consistent with the slightly higher SFR and warmer S_{60}/S_{100} colour (Table 1) in NGC 3044, leading to higher values of T_w , along with the fact that dust emission has been detected to much higher galactocentric radii (compared to the optical disk) in NGC 3044 as opposed to NGC 4157 (cf. Figs. 2d, 4d) where lower T_c might be measured.

With the above assumptions, the fraction of cold to warm dust in the galaxy, N_c/N_w (equivalent to the mass fraction, M_c/M_w), has also been computed and is listed in Table 4. Previous values for a large sample of galaxies (Dunne & Eales 2001; James et al. 2002) fall in the rather large range, $0.6 \leq N_c/N_w \leq 500$; with few exceptions, the implication is that there is much more cold than warm dust in galaxies and our results are again consistent with this conclusion.

For a two-temperature model, the dust mass can be found from

$$M_d = \frac{S_\nu D^2}{\kappa_\nu} \left[\frac{N_w + N_c}{N_w B_\nu(T_w) + N_c B_\nu(T_c)} \right] \quad (3)$$

where we take $\nu = 3.53 \times 10^{11}$ Hz (850 μm), S_ν is the flux density at this frequency, D is the distance to the galaxy, and κ_ν is the dust mass opacity coefficient at 850 μm . The value of κ_ν is uncertain since $\kappa_\nu \propto \nu^\beta$. We adopt a value of $\kappa_\nu = 0.77 \text{ cm}^2 \text{ g}^{-1}$ for consistency with other authors (Zhu et al. 2007; Vlahakis et al. 2005; Dunne & Eales 2001; Dunne et al. 2000) and in agreement with James et al. (2002). The results are listed in Table 4. These masses fall within the range found for previous galaxy samples observed at 850 μm by James et al. (2002), Dunne et al. (2000) and also when 850 μm data are included in SED fits (Willmer et al. 2009).

There is considerably more dust in NGC 3044 than NGC 4157. Some of this difference may be attributed to sensitivity differences between the two galaxies which did not enable detection of emission in NGC 4157 as far out in radius than NGC 3044 (Sect. 3.2.2). However, undetected flux at large galactocentric radii is unlikely to increase M_d of NGC 4157 by the factor of 8 which would bring it into agreement with the dust mass in NGC 3044, even if N_c/N_w were increased to account for a possibly increasing fraction

of colder dust at the larger radii. There appears to be a real difference in dust mass between the two galaxies.

The global gas/dust ratio for the two galaxies is given in Table 4 where the gas mass is the sum of M_{HI} and M_{H_2} in Table 1 and the dust mass is given in Table 4. The H_2 mass has been taken from early CO observations for which the error bars are significant; nevertheless, the difference between the two galaxies is again apparent, mainly because of the larger dust content in NGC 3044, rather than significant differences between gas masses. (We have, in addition, resolved CO(J=2-1) data for NGC 3044 from Lee (1998) which we make use of in the next section.)

3.4 Major Axis Distributions of NGC 3044

For NGC 3044, we have spatially resolved data in a number of wavebands for which we can compare the normalized major axis distributions at a common spatial resolution (21 arcsec or 2.2 kpc). Fig. 7 shows the 850 μm slice in red and the 617 MHz slice in green. We show the 850 μm data, rather than the 450 μm data, since the S/N is higher for this data set and also the data unambiguously represent the cold dust distribution (Fig. 6). A correlation between the cold dust and synchrotron emission is apparent, but there are significant differences as well: the synchrotron-emitting component is narrower in this normalized plot and also has a smoother distribution. We will return to this issue in Sect. 3.5.

In addition, we have obtained both HI and CO data for this galaxy from Lee & Irwin (1997) and Lee (1998), respectively. The CO(J=2-1) data were obtained from the JCMT at 21 arcsec resolution and the data reduction of this component follows the description in Lee et al. (2001); we take the CO(J=2-1) emission to represent the molecular gas distribution⁸. These distributions are also plotted in Fig. 7. The HI distribution is very broad in comparison to the molecular gas, the latter being strongly centrally peaked with the exception of a discrete peak at a projected radius of -60 arcsec (i.e. to the northwest). The closest correlation is between the synchrotron emission and the molecular gas distribution within the central ± 50 arcsec, indicating the well-known close association between molecular gas, star formation, and the subsequent synchrotron radiation that is produced by supernovae. A plot of total gas distribution cannot be formed since the point-by-point ratio, CO(J=2-1)/CO(J=1-0) is not available.

3.5 617 MHz - 850 μm Correlations

Following Brar, Irwin & Saikia (2003) and, as indicated in Sect. 1.2, we have searched for a correlation between the 617 MHz and 850 μm data within the two galaxies; the latter waveband was chosen because it delineates the cold dust well (see Fig. 6) and also has the highest S/N of our sub-mm data. We use the images of Figs. 2b and d and 4b and d, smoothed to matching 15 arcsec spatial resolutions, sampled at 2 pixels per beam (approximately Nyquist) and all images cut off at their respective 3σ noise levels.

⁸ Available CO(J=1-0) data are not of sufficient spatial resolution (see Solomon & Sage 1988) for comparison.

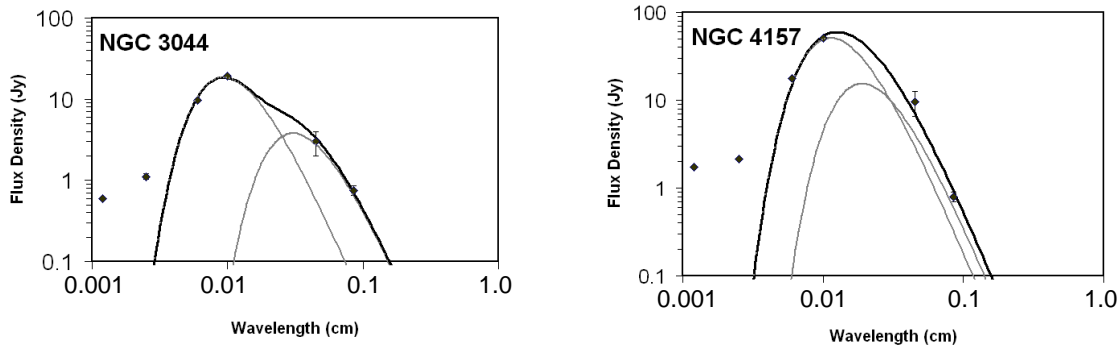


Figure 6. The spectrum of NGC 3044 (left) and NGC 4157 (right); the data points are shown with error bars. A two-temperature fit with $\beta = 2$ is shown for each. Grey curves show the warm and cold dust flux densities individually and the black curve shows the total fit (see text).

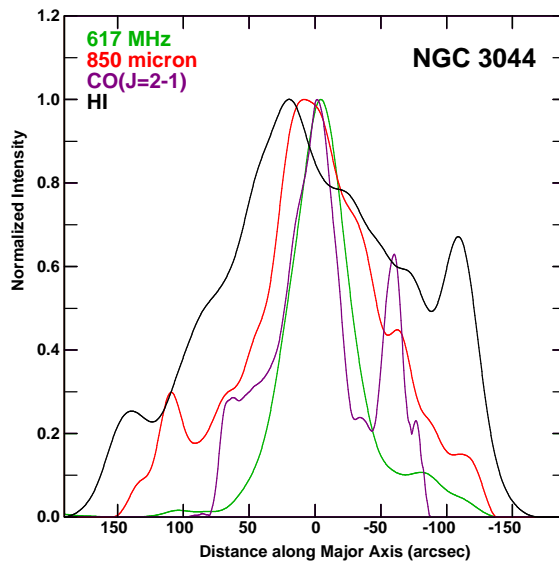


Figure 7. Comparative major axis distributions of NGC 3044 for the emission components as indicated at upper left, normalized to their respective peak values. The spatial resolution is 21 arcsec for all distributions, the galaxy emission has been rotated by -23° so that the major axis lies along the x axis and has been averaged over 21 arcsec in the minor axis direction. Positive x values lie to the south-east along the major axis. Data sources and estimated errors are: 617 MHz (this work, ± 0.004 normalized units), 850 μ m (this work, ± 0.05 normalized units), CO(J=2-1) (Lee 1998, 20%), HI (Lee & Irwin 1997, ± 0.02 normalized units).

The results are shown in Figs. 8a and c for NGC 3044 and NGC 4157, respectively, with the radio data on the y axis, as is customary. The 617 MHz and λ 850 μ m data are clearly positively correlated within the two galaxies, the correlation coefficients being 0.84 and 0.77 for NGC 3044 and NGC 4157, respectively. The scatter in the two plots exceeds the individual error bars on the points, a result which is also found for the radio continuum - FIR relation, and the extent of the scatter appears to be similar to that of the radio continuum - FIR relation, i.e. approximately a factor of 2 both within and between galaxies (e.g. Yun, Reddy & Condon 2001; Bell 2003; Hoernes et al. 1998; Hippelein et al. 2003; Murphy et al. 2006a).

We then searched for the best relation between the two

quantities using the least squares bisector approach (Isobe et al. 1990) but as applied to potentially non-linear data. Such an approach allows for the presence of a non-zero intercept, should one exist. We use a Levenberg-Marquardt algorithm to search for a power law of the form, $y = ax^\alpha + b$, which finds the best fit by minimizing the weighted sum of the squared residuals in the y coordinate. The fit is carried out in both the ‘forward’ direction (617 MHz data on the y axis) as well as the ‘reverse’ direction (λ 850 μ m data on the y axis). The results of these two best fits are shown as dashed curves in Fig. 8a and c. The best fit is then considered to be the bisector of the forward and reverse fits, where α is the average of the two fitted power law indices, the bisector passes through the crossing point of the two fits, and the

bisector is placed such that areas between it and the forward and reverse fits are minimized. The bisectors are shown as solid curves in Fig. 8a and c and their parameters are listed in Table 5.

The results of Table 5 do not change significantly if the lower cutoff is varied or if the pixel sampling is varied. For example, we have tried a lower cutoff of 2σ and also one pixel-per-beam averaging, yielding consistent results. The uncertainties are given for α , which is the most important fitted parameter (see Sect. 4), determined from the larger of the formal error of the fit and some variation that results from systematic trials with different input parameters as starting points, and finally adjusting to one pixel/beam sampling. In each case, a power law fit improved the result over a simple linear fit (i.e. χ_r^2 is lower), although, for both galaxies, the uncertainty on the power marginally encompasses the linear case ($\alpha = 1.4 \pm 0.5$ for NGC 3044 and 0.91 ± 0.08 for NGC 4157).

As indicated in Sect. 1.2, the FIR-radio continuum relation has been shown to improve when the FIR emission is smoothed. This process effectively ‘forces’ the UV photon dust optical depth to more closely match the synchrotron diffusion length. Following Murphy et al. (2008), we apply a sequence of smoothing kernels to the same $\lambda 850 \mu\text{m}$ maps used above with consecutively increasing ‘smearing scale-lengths’. A $\lambda 850 \mu\text{m}/617 \text{ MHz}$ ratio map is then formed, normalized, and the residuals compared to see which, if any, improve upon the relations plotted in Figs. 8a and c. We tried both exponential smearing kernels (e^{r/l_e}) where r is the distance from each point and l_e is the exponential scale length (both in the plane of the sky) as well as gaussian smearing kernels ($e^{r^2/2\sigma_G^2}$), where σ_G is the standard deviation of the gaussian. In both cases, a sequence of scales from 1 to 25 arcsec in 1 arcsec steps was tried. Like Murphy et al. (2008), we find that the residuals first decrease and then increase again as kernel size increases, resulting in a clear scale for which the fit is best.

The best fit results are given in Table 5 and are plotted in Figs. 8b and d. There is no doubt that the fits are improved after applying this smoothing and, moreover, that the correlation becomes non-linear ($\alpha = 2.1 \pm 0.3$ for NGC 3044 and 1.4 ± 0.3 for NGC 4157). For these cases with smoothing kernels, we also provide uncertainties on the other fitted parameters, as described above. Note that the intercept for NGC 3044 (Table 5) is consistent with zero. This is not the case for NGC 4157 although, for both galaxies, the forward and reverse bisectors encompass the (0,0) point. Since the intercept is zero for NGC 3044, we have also provided a logarithmic plot for this galaxy which is shown in Fig. 9. The best fit linear slope in this space with the displayed sampling (1.9 ± 0.1) agrees with the non-linear fit of Table 5.

We find that the Gaussian smoothing kernel produces a better fit than an exponential kernel. It has been suggested that an exponential kernel is more likely to describe a situation in which cosmic ray electrons escape from the disk whereas a Gaussian kernel would describe a random walk (Bicay & Helou 1990). For an edge-on galaxy, it is not straightforward to interpret the resulting best fit scale; however, since we are looking through a long in-disk line of sight in our two galaxies, we would expect that the in-disk (random walk) component should dominate, consistent with our

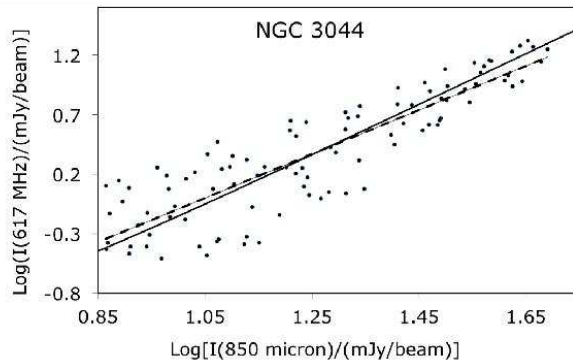


Figure 9. Logarithmic plot of the $\lambda 850 \mu\text{m}$ 617 MHz correlation for NGC 3044. The data from Fig. 8b have been replotted here without the error bars. The solid curve is the bisector from that figure and the dashed curve is the best linear fit in logarithmic space whose slope is 1.9 ± 0.1 .

better Gaussian fit. For more face-on galaxies, Murphy et al. (2006a) found that exponentials provided better fits and Marsh & Helou (1998), with earlier data, found that both Gaussians and exponentials were equally acceptable.

The non-linear relationship between the 617 MHz and $\lambda 850 \mu\text{m}$ emission explains the fact that the major axis slices for these two bands, although roughly correlated, do not follow each other particularly well in Fig. 7 (red and green curves). However, when the functional relationship shown in Fig. 8b is applied to the $\lambda 850 \mu\text{m}$ emission and renormalized, the widths of the two distributions (not shown) match each other to well within a beam size. (Note that squaring the $\lambda 850 \mu\text{m}$ emission will *narrow* its distribution, bringing it in alignment with the 617 MHz emission after normalization.) These results will be discussed further in Sect. 4.

4 DISCUSSION

4.1 High-Latitude Emission

4.1.1 NGC 3044

The presence of a multi-phase gaseous halo in NGC 3044 has been known for some time (Hummel & van der Hulst 1989; Condon et al. 1990; Colbert et al. 1996; Irwin, English & Sorathia 1999; Irwin, Saikia & English 2000; Collins et al. 2000; Tüllmann & Dettmar 2000; Miller & Veilleux 2003; Tüllmann et al. 2006; Lee & Irwin 1997). See Collins et al. (2000), for example, for measurements of the HI and eDIG scale heights in this galaxy. Our new observations are the first at 617 MHz and $\lambda 850 \mu\text{m}$ and reveal several new high latitude features in these two wavebands (Fig. 2 and Sect. 3.1.1).

These disturbances are better seen in several selected overlays shown in Fig. 10; the greyscales show H α emission, HI total intensity emission, and smoothed H α emission in frames a, b, and c, respectively. At a location of about 1.5 arcmin from the nucleus along the north-west major axis there is a gap in the H α emission in the disk (Fig. 10a). At this position is an HI supershell, part of which is visible as the high latitude feature, F10 (Fig. 10b), so labelled by Lee & Irwin (1997). The narrow vertical dust feature observed at

Table 5. Parameters of the 617 MHz - λ 850 μ m Correlations

σ_G^b	NGC 3044 ^a				σ_G^b	NGC 4157 ^a			
	a^c	a^c	b^c	$\chi_r^2{}^d$		a^c	a^c	b^c	$\chi_r^2{}^d$
8'' (0.84 kpc)	0.06	1.4 \pm 0.5	-1.3	7.55	10'' (0.63 kpc)	0.046	0.91 \pm 0.08	-1.9	7.34
	0.005 \pm 0.003	2.1 \pm 0.3	0.04 \pm 0.2	3.06		0.07 \pm 0.05	1.4 \pm 0.3	1.5 \pm 0.5	4.9

^a An equation of the form, $S_{617} = a S_{850}^\alpha + b$ has been applied, where S_{617} and S_{850} are the 617 MHz and 850 μ m flux densities, respectively, in mJy beam⁻¹.

^b Standard deviation of the Gaussian smoothing kernel applied to the λ 850 μ m data. Blank means no smoothing.

^c Fitted parameters as defined in *a* above.

^d Reduced χ^2 , i.e. weighted sum of the squared residuals in the y coordinate, normalized by the number of degrees of freedom.

λ 850 μ m, although at a low S/N, occurs adjacent to F10 and the double-pronged 617 MHz feature is also at this position. Apparently, there is disturbance in the disk at this location which is affecting all of the components displayed and that disturbance has excavated an ionized gas cavity in the disk. This is not the first time that high latitude features have been associated with a gap or absence of H α emission in the underlying disk; see Lee et al. (2001) for another prominent example in NGC 5775.

On the whole, there is global correspondence between the radio continuum and H α emission as seen in Fig. 10c). This correspondence, which has been pointed out by many authors, including Collins et al. (2000) for NGC 3044 itself, can be understood from the fact that both components are associated with massive star formation.

What is more unusual, as pointed out in Sect. 3.1.1, are the extraplanar features which appear to originate at the two ends of the major axis. In particular, at the south-east end, the emission is truncated approximately where the H α emission also narrows abruptly (Fig. 10c). We then see a series of disconnected emission features in *both* the GMRT 617 MHz and VLA 20 cm images (Figs. 2b and 3b, respectively), including the feature at RA \approx 9^h 53^m 51^s, DEC \approx 01 $^\circ$ 35' 45'' which we have labelled the non-thermal cloud (NTC) in Fig. 2b. The feature centers at approximately 2 arcmin (13 kpc) from the galaxy's major axis.

In Fig. 11 we show the 617 MHz (red contours) and λ 20 cm (blue dashed contours) emission of NGC 3044 superimposed on a greyscale image of the λ 22 μ m emission taken from the Wide-field Infrared Survey Explorer (WISE) all sky survey (Wright et al. 2010; Cutri et al. 2012), the latter enhanced to show low intensities that are $> 2\sigma$ in brightness. The λ 22 μ m emission is an indicator of the presence of warm dust (of order 130 K for classical grains in thermal equilibrium). This map shows that the halo of NGC 3044 is even more extensive than previously known and shows considerable substructure, including vertical extensions and arcs as well as 'disconnected' features towards the north. It is beyond the scope of this paper to discuss the WISE results in detail; however, when considered together with the two independent radio continuum maps (GMRT and VLA), the results give credence to the reality of the northwards extensions that begin on the south-east end of the major axis. Note that, at low S/N, sensitivity to spatial scales (which depends on an array's uv coverage) is as important as S/N in determining what emission features will be detected. Consequently, the GMRT and VLA emission, while overlapping,

do not align perfectly and should not be used to determine spectral indices at these low emission levels. Put together, though, the truncation of the radio continuum major axis where the northwards extension begins, the abrupt narrowing of the H α emission at this position, and emission extending towards the north that is visible in GMRT 617 MHz, the VLA λ 20 cm map, and the WISE λ 22 μ m map, suggest that a disruption has occurred at the south-east end of the major axis in this galaxy and expelled material to the north of the plane.

Bearing in mind the low S/N of the NTC, if we nevertheless take it at face value, we can estimate some physical parameters. Excluding the smaller features closer to the major axis, the NTC, as shown in Fig. 2b, has a flux density of 3 mJy, or a spectral power of $P_{617\text{ MHz}} = 1.7 \times 10^{20}$ W/Hz. By comparison, the flux density of the Galactic supernova remnant, Cas A, is $S_{617}(\text{Cas A}) = 3425.4$ Jy for epoch 2005.5 (Vinyaikin 2007), corresponding to $P_{617\text{ MHz}} = 4.7 \times 10^{18}$ W/Hz at its distance of 3.4 kpc (Hammell & Fesen 2008). Thus, the radio power of the NTC alone corresponds to 36 equivalent supernova remnants. If we include features closer to the disk, the value approximately doubles. The environment of the NTC differs substantially from that of Cas A; nevertheless this comparison suggests that a massive star-forming region in the disk could indeed have been responsible for the observed emission from the point of view of energetics.

Regarding timescales, from the mean magnetic field strength ($\bar{B} = 5.8 \mu\text{G}$) found throughout the disk and the observed halo of NGC 3044 (Irwin, English & Sorathia 1999), the mean cosmic ray electron lifetime is $\tau_{CR} = 6.5 \times 10^7$ yr (see Sect. 4.1.3). However, the magnetic field was found to vary from 3.5 to 8.9 μG and it is likely that CRs far from the disk would be associated with magnetic fields that are at the low end of this range. Consequently, a lifetime of $\tau_{CR} = 1.4 \times 10^8$ yr ($\tau_{CR} \propto B^{-3/2}$) may be more appropriate. For a distance of 13 kpc, then, the outflow velocity would be 91 km s⁻¹ which is much less than the 300 km s⁻¹ outflow velocity observed in NGC 253 by Heesen et al. (2009), for comparison.

The above calculations are order of magnitude only and are meant to illustrate the feasibility of non-thermal emission far from the disk of NGC 3044 having originated from activity within the disk. We require more information on the magnetic field distribution and strength to make more definitive statements.

As noted earlier, the 617 MHz emission in NGC 3044

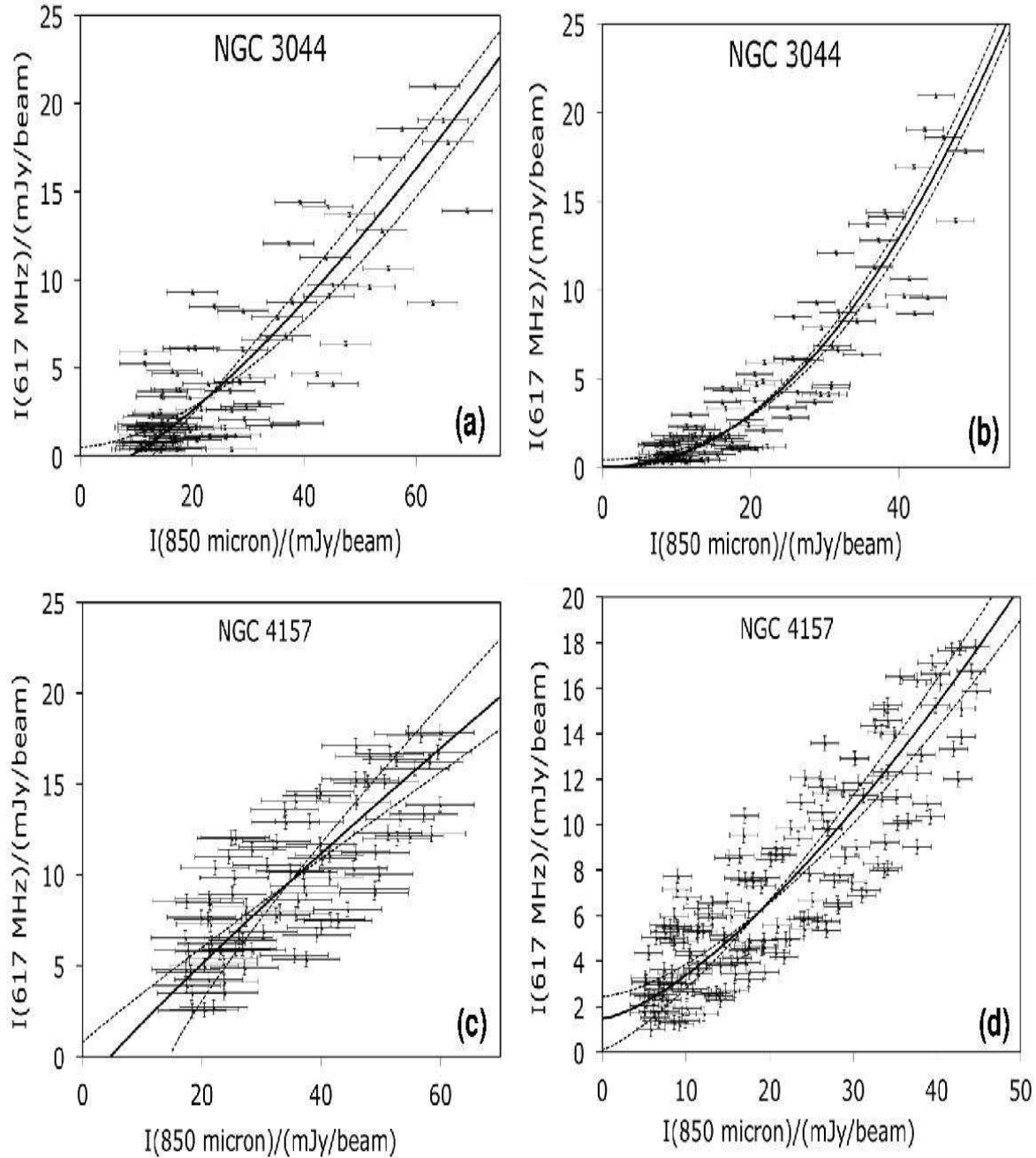


Figure 8. Correlations between the $\lambda 850 \mu\text{m}$ and 617 MHz specific intensities for each galaxy at 15 arcsec resolution and with each data set cut off below its respective 3σ levels. Points with error bars are the measured values. The two curved dotted lines are best fit functions of the form, $y = ax^\alpha + b$, in the forward [$y=f(x)$] and reverse [$x=f(y)$] directions, respectively (see Sect. 3.5), and the solid curves represent the bisector power law relations in each case. (a) NGC 3044, with no smoothing. (b) NGC 3044, in which the $\lambda 850 \mu\text{m}$ image has been smoothed with a Gaussian kernel of standard deviation, $\sigma_G = 8$ arcsec. (c) NGC 4157, with no smoothing. (d) NGC 4157, in which the $\lambda 850 \mu\text{m}$ image has been smoothed with a Gaussian kernel of standard deviation, $\sigma_G = 10$ arcsec.

shows curvature towards the north on both ends of the major axis of NGC 3044 which sometimes suggests that ram pressure stripping could be occurring as the galaxy passes through an intergalactic medium (IGM) in a southerly direction. However, there is no such evidence in the HI emission and, in fact, HI extensions are observed on both the north and south sides of the major axis. In addition, the isovelocity HI contours show a slight curvature which, if caused by

motion through an IGM, would imply a motion to the north-east rather than the south-west (see Fig. 4 of Lee & Irwin 1997). This suggests that the observed 617 MHz extensions at the ends of the major axis and the disconnected northern features may have been produced from internal activity which is asymmetrically placed with respect to gas distribution (or magnetic field distribution) in the galaxy. Lee & Irwin (1997) also argue for an internal origin for the HI su-

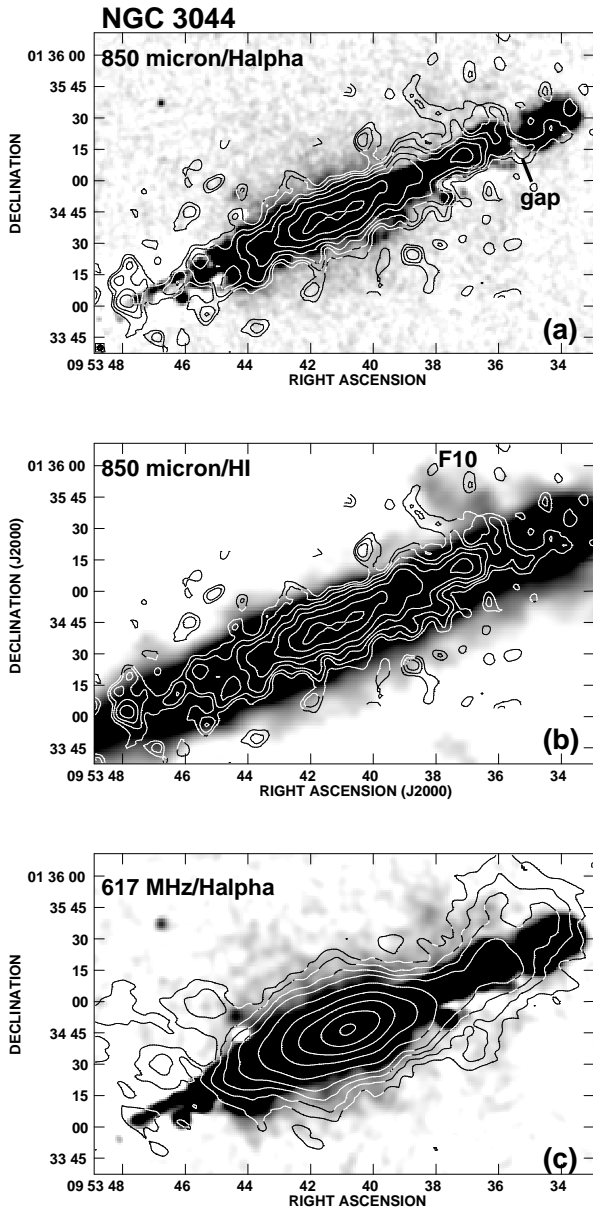


Figure 10. Selected overlays for NGC 3044 showing extraplanar emission. (a) $\lambda 850 \mu\text{m}$ contours as in Fig. 2d, over a greyscale H α image from Collins et al. (2000). The H α ‘gap’ in the major axis that is discussed in Sect. 4.1.1 is labelled. (b) $\lambda 850 \mu\text{m}$ contours as in Fig. 2d, over a greyscale HI total intensity map from Lee & Irwin (1997), where F10 denotes an HI extension identified as part of an expanding shell in the latter reference. (c) 617 MHz contours as in Fig. 2b over a greyscale H α image from Collins et al. (2000) smoothed to 5 arcsec resolution.

pershells and the energetics (above) are consistent with this. With distributed star formation in the galaxy, it is reasonable to expect that outflows will more effectively eject material far from the plane at large galactocentric radii where the internal disk density is lower.

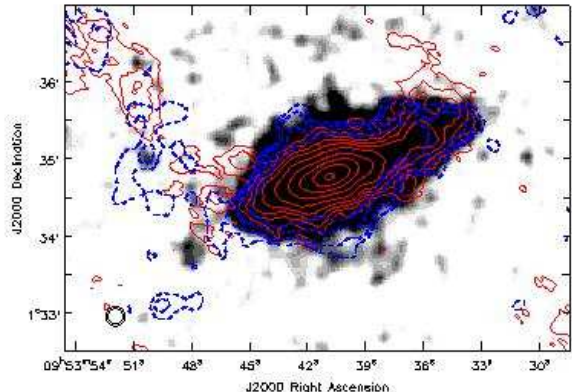


Figure 11. The 617 MHz emission (red contours) from Fig. 4b, and the $\lambda 20$ cm emission (blue dashed contours) from Fig. 5b, are shown overlaid on a greyscale of the WISE $\lambda 22 \mu\text{m}$ emission. The WISE image has been cut off at the 2σ level and is shown so as to enhance the faint broad-scale emission.

4.1.2 NGC 4157

NGC 4157 is also known to exhibit high latitude emission (Irwin, English & Sorathia 1999; Kennedy 2009) but fewer observations of this galaxy have been carried out in comparison to NGC 3044. As seen in Figs. 4c and d, we do not have sufficient S/N for a clear detection of high latitude dust in NGC 4157. The radio continuum emission (Figs. 4a and b) shows some extensions that are roughly at the locations of those seen in the VLA 20 cm map (Fig. 5). A new feature is seen in the 617 MHz map (Fig. 4b) in the form of a radio continuum extension beginning at the far north-eastern end of the major axis and extending south, as described in Sect. 3.2.1.

This southern extension can be better seen in Fig. 12 where it is overlaid onto a greyscale image of the $\lambda 22 \mu\text{m}$ WISE emission. This plot shows that warm dust exists in a halo that extends up to 1.3 arcmin (4.9 kpc) from the plane. The HI in this galaxy extends to roughly the same z distance Kennedy (2009) (although HI also extends much farther in the radial direction along the major axis). The dust, therefore, may be a component of the high-latitude HI in the same way that it normally is within a galaxy disk.

For the purposes of our 617 MHz comparison, we note that the southern 617 MHz extension coincides with discrete dust emission in roughly the same direction which gives weight to our assertion that the extension is real. Indeed, some of the 617 MHz features on the north side of the disk also have dust counterparts. Although it isn’t clear whether these features occupy the same volume, the evidence continues to mount that all constituents of the ISM are represented in galaxy halos. See Lee et al. (2001) for an earlier example.

4.1.3 The Non-thermal - Cold Dust Relation in NGC 3044

As can be seen from Fig. 6, the $\lambda 850 \mu\text{m}$ emission in NGC 4157 (as modeled) still includes a contribution from the warm dust component whereas the emission of NGC 3044 is strongly dominated by only cold dust at that

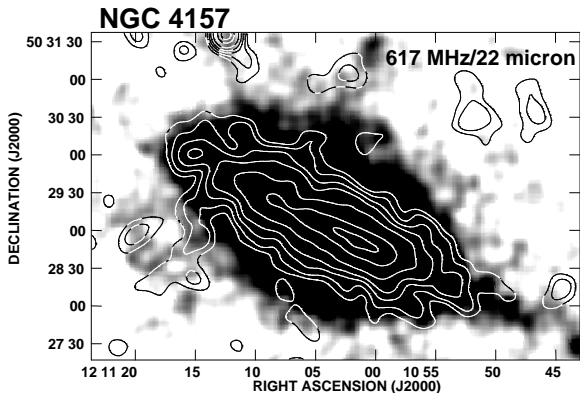


Figure 12. Contours of GMRT 617 MHz emission as in Fig. 4b over a greyscale WISE image at $\lambda 22 \mu\text{m}$. The WISE image (spatial resolution of 12 arcsec) has been cut off at 2σ and is shown so as to enhance the faint broad-scale emission.

wavelength. In addition, the S/N of the NGC 3044 data is higher than that of NGC 4157. We therefore consider only NGC 3044 in our discussion of the 617 MHz - $\lambda 850 \mu\text{m}$ relation which we take to represent a relationship between synchrotron emission and cold dust ($T_c = 9.5 \pm 1.5 \text{ K}$, Table 4).

Firstly, we note that the relationship between these two components is significantly improved when a smearing kernel is introduced to the sub-mm data (Fig. 8), consistent with earlier results (Murphy et al. 2006a,b, 2008, 2009). This kernel ‘corrects’ for differences between the photon mean free path to dust absorption and the CR electron diffusion length. We find, not only that the correlation improves, but also that it becomes clearly non-linear such that $S_{617 \text{ MHz}} \propto S_{850 \mu\text{m}}^{2.1 \pm 0.2}$; that is, the relationship is roughly consistent with a luminosity relation of $L_{\text{synch}} \propto L_{\text{cold dust}}^{2.1}$. By comparison, Pierini et al. (2003) found $L_{1.4 \text{ GHz}} \propto L_{\text{cold dust}}^{1.13}$ and Brar, Irwin & Saikia (2003) found a roughly linear 617 MHz - $\lambda 850 \mu\text{m}$ relation for NGC 5775. Neither of these authors applied a smearing kernel and, as Fig. 8 illustrates, the correlation becomes much flatter ($S_{617 \text{ MHz}} \propto S_{850 \mu\text{m}}^{1.4 \pm 0.3}$, Table 4), when a smoothing kernel is ignored.

Murphy et al. (2006b) have shown that galaxies with higher SFRs per unit area have lower kernel scale lengths. They interpret this result to imply that galaxies with high SFRs contain, on average, younger SF regions from which CR electrons have not had sufficient time to diffuse to large scales. When SF has not been so recent, by contrast, the difference between the radio continuum scale and the dust scale diminishes.

As indicated in Sect. 3.5, it is not straightforward to interpret the meaning of the kernel size for an edge-on galaxy in which the line of sight that is being probed varies with position and may probe a range of SF regions of varying ages. In addition, our best result corresponds to a gaussian kernel which cannot be directly compared to the exponentials used by Murphy et al. (2006b) in more face-on systems. Nevertheless, we can consider some representative timescales to

see whether our kernel size could reasonably represent a link between the CR electron and dust heating scales.

For example, based on spatially resolved images at $\lambda 20 \text{ cm}$ and $\lambda 6 \text{ cm}$, the minimum energy magnetic field strength in NGC 3044 has a mean value of $B = 5.8 \mu\text{G}$, ranging from 3.5 to 8.9 μG to within uncertainties of approximately a factor of 2 (Irwin, English & Sorathia 1999). The lifetime for cosmic ray electrons against synchrotron and inverse Compton losses, for an isotropic velocity distribution of CR electrons, is given by (e.g. Murphy et al. 2006b),

$$\left(\frac{\tau_{\text{CRE}}}{\text{yr}}\right) \sim \frac{5.7 \times 10^7 \left(\frac{B}{\mu\text{G}}\right)^{0.5}}{\left(\frac{\nu}{\text{GHz}}\right)^{0.5} \left(\frac{u_B + u_{\text{rad}}}{10^{-12} \text{ ergs cm}^{-3}}\right)} \quad (4)$$

where B is the magnetic field strength and u_B and u_{rad} are the magnetic field and radiation energy densities, respectively.

Taking $u_B = B^2/(8\pi)$ and $u_B \approx u_{\text{rad}}$, then $\tau \propto B^{-3/2}$ and we find $\tau = 6.5 \times 10^7 \text{ yr}$ (ranging from 3.3 to $14 \times 10^7 \text{ yr}$). This implies that the 617 MHz emission is measuring a massive SF history of NGC 3044 that is integrated over 10^{7-8} yr ; it is not measuring the recent SF activity in the galaxy.

In this time, how far can CR electrons diffuse? The diffusion timescale can be written (Murphy et al. 2009),

$$\left(\frac{\tau_{\text{diff}}}{\text{yr}}\right) = 2 \times 10^6 \left(\frac{l_{\text{diff}}}{\text{kpc}}\right)^2 \left(\frac{\nu}{\text{GHz}}\right)^{-0.25} \left(\frac{B}{\mu\text{G}}\right)^{0.25} \quad (5)$$

where l_{diff} represents the distance that a CR electron can diffuse from its point of origin via a random walk, assuming an energy-dependent diffusion coefficient. Setting $\tau_{\text{CRE}} = \tau_{\text{diff}}$ yields $l_{\text{diff}} = 4.3 \text{ kpc}$. This is a significant distance and sufficient to allow CR electrons to ‘fill’ the galaxy disk, assuming that SF has been widely distributed over the past 10^{7-8} yr .

If the cold dust is heated by the ISRF which is similarly widely distributed throughout the disk then, at least to order of magnitude, our smoothing kernel should represent roughly the difference between the CR electron diffusion length and the dust mean free path to ISRF photons. The latter is not known for NGC 3044 (and likely varies), but in our own Galaxy, a typical dust cross-section to absorption and scattering in the visible through UV part of the spectrum for big grains, σ_H , ranges from 0.2 to $1 \times 10^{-21} \text{ cm}^2$ per hydrogen atom (Désert, Boulanger & Puget 1990). For this range of dust cross-section and using the mean ISM gas density in NGC 3044 of $n_H \approx 0.25 \text{ cm}^{-3}$ (Lee & Irwin 1997), the mean free path of ISRF photons to dust is $l_{\text{dust}} = 1.3 \rightarrow 6.5 \text{ kpc}$.

Our Gaussian smoothing kernel of $\sigma_G = 0.84 \text{ kpc}$ (Table 5) corresponds to a radius (half-width at half maximum) of $l_G = 1.0 \text{ kpc}$. If we convolve this size scale with l_{dust} , the result is $l_{\text{dust-conv}} = 1.6 \rightarrow 6.6 \text{ kpc}$ which can now be compared to $l_{\text{diff}} = 4.3 \text{ kpc}$ estimated above. Although there are many uncertainties and assumptions in this comparison, the result indicates that the interpretation of the smoothing kernel as accounting for the difference between the CR electron diffusion scale and the photon mean free path to dust is reasonable.

Our results suggest that there is a clear link between synchrotron emission, which measures the integrated mas-

sive SF history in the galaxy over a few 10^{7-8} yr, and the ISRF-heated cold dust. In the latter case, the fraction of heating that is due to FUV photons from young massive stars is uncertain (e.g. see the discussion in Bell 2003). Older stars contribute approximately an order of magnitude more photons than OB stars in the Solar neighbourhood (Tielens 2006, p. 13) whereas the cross-section for large grains increases by only a factor of 5 from the infrared through the ultraviolet (Désert, Boulanger & Puget 1990). In addition, we are considering emission from regions (of order 4.3 kpc, see above) which are much larger than typical regions within which hot massive stars exist; the heating source for the λ 850 μ m dust emission over such size scales is then the cooler stellar population (as has been found by other authors previously), rather than the hot, young massive stars that eventually give rise to the synchrotron emission via supernovae.

What then is the connection and the reason for the non-linear relation? We first note that non-linear relations have been observed before, especially when considering those of lower luminosity ($L_{IR} \lesssim 10^{10} L_{\odot}$) and/or galaxies that have been studied at low radio frequencies ($\nu \lesssim 5$ GHz). In such cases, the relation $L_{radio} \propto L_{IR}^{\gamma}$, where $\gamma > 1$ has been observed. Such a trend has been interpreted as reflecting an increasing contribution from older stars in heating the dust, a non-linear relation between the SFR and radio continuum emission, or an underproduction of both radio and infrared emission in low luminosity galaxies (see e.g. Bell 2003).

To our knowledge, however, a slope as steep as $\gamma = 2.1$ has not previously been observed, likely because of the lack of smoothing as described above. The closest comparisons are to the results of Brar, Irwin & Saikia (2003) and Horner et al. (1998) for NGC 5775 and M 31, respectively, who both find approximately linear relations between non-thermal radio emission and cold dust, in agreement with our result when a smoothing kernel is ignored.

For both the 617 MHz and λ 850 μ m emission, we are observing optically thin emission over equivalent lines of sight. Then the relation compares the emissivities of the two components (see also Groves et al. 2003). For synchrotron emission, the emission coefficient can be expressed as,

$$j_{synch} \propto n_{CRE} B^{\frac{\Gamma+1}{2}} \quad (6)$$

where n_{CRE} represents number density of CR electrons, B is the magnetic field strength (we take $B_{\perp} \propto B$), and Γ is the power law slope of the CR electron spectrum.

There is substantial observational and theoretical evidence for an approximately constant Alfvén speed in the ISM leading to $B \propto \sqrt{n_g}$, where n_g is the gas density (Troland & Heiles 1986; Chaboyer & Henriksen 1990; Groves et al. 2003; Thompson, Quataert, & Murray 2009, and others). In addition, we expect that $n_{CRE} \propto SFR_m$, where SFR_m is the massive SFR. If we accept that the massive SFR is governed by a Schmidt law such that $SFR_m \propto n_g^{\eta}$, then the above equation becomes,

$$j_{synch} \propto n_g^{\frac{4\eta+\Gamma+1}{4}} \quad (7)$$

For the dust emissivity, we have,

$$j_{cold\ dust} \propto n_d B_{\nu}(T_c) \quad (8)$$

which is essentially a variant of Eqn. 1 in which the optical

depth is expressed explicitly as a function of the number density of dust grains (n_d). If we take a constant gas/dust ratio, then $n_d \propto n_g$. In addition, variations in gas density in the ISM can be many orders of magnitude, whereas a reasonable variation in the cold dust temperature results in a variation in $B_{\nu}(T_c)$ of factors of a few (e.g. increasing the error bar on T_c for NGC 3044 by a factor of two varies $B_{\nu}(T_c)$ by a factor of approximately ± 2). Dust temperatures may vary a great deal in the ISM, but since we are considering only the λ 850 μ m emission which we have linked to the cold dust of NGC 3044 only, we will assume that gas density variations dominate and approximate the cold dust emission as,

$$j_{cold\ dust} \propto n_g \quad (9)$$

Another way of expressing the above is that the ISRF imposes an essentially constant heating effect on $j_{cold\ dust}$ due to a presumed dominance of widespread and long-lived cooler stars to this heating.

Combining Eqns. 7 and 9 and restoring the flux nomenclature yields,

$$S_{617} \propto S_{850}^{\frac{4\eta+\Gamma+1}{4}} \quad (10)$$

Taking the observational results for the Schmidt law summarized by Kennicutt (2008), i.e. $\eta = 1.4 \pm 0.1$, and using the mean spectral index between λ 20 and 6 cm measured by Irwin, English & Sorathia (1999) for NGC 3044, $\bar{\alpha} = -0.6$, leading to $\Gamma = 1 - 2\alpha = 2.2$, we find,

$$S_{617} \propto S_{850}^{2.2} \quad (11)$$

which agrees with the measured $S_{617} \propto S_{850}^{2.1 \pm 0.2}$ for NGC 3044, within errors. See Niklas & Beck (1997) for an earlier example of this kind of approach.

It is important to note the variations that can occur in the above indices. The measured spectral index of NGC 3044, for example, ranges from -1.0 to 0.2 within the galaxy and may differ from these values at the lower frequency that has been used in these observations. As for the Schmidt law, theoretical considerations result in values that can generally be found in the range, $\eta = 1 \rightarrow 2$ (Larson 1992), though a free-fall value yields $\eta = 1.5$ (Henriksen 1991, his Eqn. 38). Observationally, variations in η are also observed (Bigiel 2008; Kennicutt & Evans 2012). Nevertheless, the above result shows that a simple application of the average spectral index and the most universally accepted Schmidt law provides a reasonable explanation for the 617 MHz - 850 μ m correlation found in NGC 3044. For this result, it is important that the non-thermal radio emission and cold dust emission are sufficiently isolated spectrally and that the dust scale length is adjusted through smoothing.

To summarize, if we assume a constant ISRF heating of the cold dust, then the link between synchrotron emission and cold dust is via the gas density. A higher gas density yields a higher SFR and a higher magnetic field, both of which affect the synchrotron emission, and a higher gas density yields a higher dust density leading to a higher cold dust emission.

5 CONCLUSIONS

We have observed the edge-on galaxies, NGC 3044 and NGC 4157 at 617 MHz using the GMRT and at $\lambda 450$ and $\lambda 850 \mu\text{m}$ using the JCMT. These are the first results for these two galaxies at these wavelengths. The main results are as follows.

- For NGC 3044, high latitude emission is observed at 617 MHz, consistent with previous radio continuum results and some evidence is present at low intensities for vertical extensions at $\lambda 850 \mu\text{m}$ also.

- At the far ends of the major axis of NGC 3044, there appear to be disturbances which have resulted in 617 MHz emission extending away from the plane towards the north. The most most obvious of these begin on the far south-east end of the major axis, including some 'disconnected' features, one of which we have named the non-thermal cloud (NTC). Order-of-magnitude calculations suggest that the NTC could have originated from activity related to star-formation in the galaxy's disk. Another radio continuum extension is seen on the NW end of the major axis at which an HI supershell is known. Such disturbances will be more effective at ejecting material away from the plane if they are at large galactocentric radii where the disk density is lower.

- Some high latitude 617 MHz emission is observed in NGC 4157 but we do not have the sensitivity to unambiguously detect halo dust emission at either $\lambda 450 \mu\text{m}$ or $\lambda 850 \mu\text{m}$ for this galaxy. A large radio continuum extension is seen towards the south beginning at the end of the north-eastern major axis in this galaxy and appears to correlate with high-latitude emission seen at $\lambda 22 \mu\text{m}$ from the WISE satellite.

- We could not fit a single temperature model to the sub-mm spectrum for either NGC 3044 or NGC 4157, but could fit both spectra with a two-temperature model. For NGC 3044, we find $T_w = 31.0 \pm 1.4$ K and $T_c = 9.5 \pm 1.5$ K and for NGC 4157, we find $T_w = 25.6 \pm 1.4$ K and $T_c = 15.3 \pm 1.5$ K. For the latter galaxy, we do not detect emission at the largest galactocentric radii. Dust masses are $M_d = (1.6 \pm 0.6) \times 10^8 M_\odot$ and $M_d = (0.21 \pm 0.06) \times 10^8 M_\odot$ for NGC 3044 and NGC 4157, respectively. There is more cold than warm dust in both galaxies.

- We find a clear correlation between the 617 MHz and $\lambda 850 \mu\text{m}$ emission for both NGC 3044 and NGC 4157. This correlation improves significantly if a smoothing kernel is applied to the $\lambda 850 \mu\text{m}$ data to account for differences between the mean free path of a dust-heating photon and the diffusion length of CR electrons in the ISM. Simple timescale and length scale arguments suggest that such a smoothing kernel can indeed account for these differences.

- With an applied smoothing kernel, the 617 MHz and $\lambda 850 \mu\text{m}$ correlation becomes strongly non-linear. For the best data set and the one in which the $\lambda 850 \mu\text{m}$ is strongly dominated by cold dust (i.e. NGC 3044), we find $S_{617} \propto S_{850}^{2.1 \pm 0.2}$.

- The non-linear relation between synchrotron emission and cold dust can be understood if the heating of the cold dust is the ISRF in which cooler stars (rather than hot young stars) dominate, leading to variations in cold dust emission that are dominated by density rather than temperature variations. Synchrotron emission depends on the magnetic field strength and CR electron generation, both of which depend

on gas density via $B \propto \sqrt{\rho}$ and the Schmidt law, respectively. With these assumptions, $S_{617} \propto S_{850}^{2.2}$ which agrees with the observed correlation.

ACKNOWLEDGMENTS

This research has made use of the NASA/IPAC Extragalactic Database (NED) which is operated by the Jet Propulsion Laboratory, California Institute of Technology, under contract with the National Aeronautics and Space Administration. We are grateful to Dr. Rob Swaters for providing WHISP data and to Dr. Siow-Wang Lee for providing HI and CO(J=2-1) data. Thanks also to R. Rand for providing the H α image. The CO(J=1-0) data were originally provided by G. Golla for comparative purposes. We are especially grateful to Loretta Dunne for insightful comments.

REFERENCES

- Ade, P. A. R., et al. 2011, *A&A*, 536, 16
 Alton, P. B., et al. 1998, *ApJ*, 507, L125
 Alton, P. B., et al. 2000, *A&A*, 356, 795
 Ananthakrishnan, S. 2005, *Proc. of the Int. Cosmic Ray Conf.*, 10, 125
 Bell, E. F. 2003, *ApJ*, 586, 794
 Bendo, G. J., et al. 2002, *AJ*, 123, 3067
 Bica, M. D., & Helou, G. 1990, *ApJ*, 362, 59
 Bigiel, F. et al. 2008, *AJ*, 136, 2846
 Brar, R. S., Irwin, J. A., & Saikia, D. J. 2003, *MNRAS*, 340, 269
 Bregman, J. R., & Pildis, R. A. 1994, *ApJ*, 420, 570
 Chaboyer, B., & Henriksen, R. N. 1990, *A&A*, 236, 275
 Colbert, E. J. M., et al. 1996, *ApJ*, 467, 551
 Collins, J. A., Rand, R. J., Duric, N., & Walterbos, R. A. M. 2000, *ApJ*, 536, 645
 Condon, J. J. 1987, *ApJS*, 65, 485
 Condon, J. J., Helou, G., Sanders, D. B., & Soifer, B. T. 1990, *ApJS*, 73, 359
 Cutri, R. M., et al. 2012, *Explanatory Supplement to the WISE All-Sky Data Release Products* <http://wise2.ipac.caltech.edu/docs/release/allsky/expsup/index.html>
 de Jong, T., Klein, U., Wielbinski, R., & Wunderlich, E. 1985, *A&A*, 147, 6
 de Vaucouleurs, G., de Vaucouleurs, A., Corwin, H. G., Jr., et al. 1991, *Third Reference Catalogue of Bright Galaxies (RC3)* (Springer Verlag)
 Désert, F.-X., Boulanger, F., & Puget, J. L. 1990, *A&A*, 237, 215
 di Francesco, J., et al. 2008, *ApJS*, 175, 277
 Dunne, L., & Eales, S. A. 2001, *MNRAS*, 327, 697
 Dunne, L., et al. 2000, *MNRAS*, 315, 115
 Dupac, X., et al. 2003, *MNRAS*, 344, 105
 Eales, S. A., & Edmunds, M. G. 1996, *MNRAS*, 280, 1167
 Fraternali, F., Cappi, M., Sancisi, R., & Oosterloo, T. 2002, *ApJ*, 578, 109
 Garcia, A. M. 1993, *A&AS*, 100, 47
 Gil de Paz, A., et al. 2007, *ApJS*, 173, 185
 Gioia, I. M., & Fabbiano, G. 1987, *ApJS*, 63, 771
 Groves, B. A., Jungyeon, C., Dopita, M., & Lazarian, A. 2003, *PASA*, 20, 252

- Hammell, M. C., & Fesen, R. A. 2008, *ApJS*, 179, 195
- Heesen, V., Beck, R., Krause, M., & Dettmar, R.-J. 2011, *A&A*, 535, 79
- Heesen, V., Beck, R., Krause, M., & Dettmar, R.-J. 2009, *A&A*, 494, 563
- Helou, G., Soifer, B. T., & Rowan-Robinson, M. 1985, *ApJ*, 298, 7
- Helou, G., & Bica, M. D. 1993, *ApJ*, 415, 93
- Henriksen, R. N. 1991, *ApJ*, 377, 500
- Hippelein, H. et al. 2003, *A&A*, 407, 137
- Hoernes, P., Berkhuijsen, E. M., & Xu, C. 1998, *A&A*, 334, 57
- Holland, W. S., et al. 1999, *MNRAS*, 303, 659
- Holk, J. C., & Savage, B. D. 1999, *AJ*, 117, 2077
- Hummel, E., & van der Hulst, J. M. 1989, *A&AS*, 81, 51
- Hummel, E., Beck, R., & Dettmar, R.-J. 1991, *A&AS*, 87, 309
- Ipavich, F. M. 1975, *ApJ*, 196, 107
- Irwin, J. A., et al. 2012, *AJ*, submitted
- Irwin, J. A., English, J., & Sorathia, B. 1999, *AJ*, 117, 2102
- Irwin, J. A., & Saikia, D. J. 1999, *MNRAS*, 346, 977
- Irwin, J. A., Saikia, D. J., & English, J. 2000, *AJ*, 119, 1592
- Irwin, J. A., & Madden, S. C. 2006, *A&A*, 445, 123
- Isobe, T., Feigelson, E. D., Akritas, M. G., & Babu, G. J. 1990, *ApJ*, 364, 104
- James, A., Dunne, L., Eales, S., & Edmunds, M. G. 2002, *MNRAS*, 335, 753
- Jenness, T., & Lightfoot, J. F. 1999, The SURF Programming Interface, Starlink System Note 72
- Kennedy, H. J. 2009, Investigation of Neutral Hydrogen in Three Edge-on Spiral Galaxies, MSc Thesis, Queen's University, Canada, available at <http://hdl.handle.net/1974/5134>
- Kennicutt, R. C., Jr. 1998, *ARAA*, 36, 189
- Kennicutt, R. C., Jr. 2008, Pathways Through an Eclectic Universe, ASP Conf. Series, Vol. 390, Ed. J. H. Knapen, T. J. Mahoney, & A. Vazdekis, San Francisco, ASP, p. 149
- Kennicutt, R. C., Jr., & Evans II, N. J. 2012, *ARAA*, 50, 531
- Komugi, S., et al. 2008, *ApJS*, 178, 225
- Larson, R. B. 1992, in *Star Formation in Stellar Systems*, ed. G. Tenorio-Tagle, M. Prieto, & F. Sánchez (Cambridge: Cambridge Univ. Press), 125
- Lee, S.-W. 1998, The Interstellar Medium and Disk-Halo Interaction of the Edge-on Galaxies NGC 3044 and NGC 5775, PhD Thesis, Queen's University, Canada
- Lee, S.-W., & Irwin, J. A. 1997, *ApJ*, 490, 247
- Lee, S.-W., et al. 2001, *A&A*, 377, 759
- Marengo, M., et al. 1997, *A&A*, 322, 924
- Masi, S., et al. 1995, *ApJ*, 452, 253
- Marsh, K. A., & Helou, G. 1998, 493, 121
- Miller, S. T., & Veilleux, S. 2003, *ApJS*, 148, 383
- Murphy, E. J., et al. 2006a, *ApJ*, 638, 157
- Murphy, E. J., et al. 2006b, *ApJ*, 651, L111; Erratum 2008, *ApJ*, 672, L85
- Murphy, E. J., Helou, G., Kenney, J. D. P., Armus, L., & Braun, R. 2008, *ApJ*, 678, 828
- Murphy, E. J., Kenney, J. D. P., Helou, G., Chung, A., & Howell, J. H. 2009, *ApJ*, 694, 1435
- Niklas, S., & Beck, R. 1997, *A&A*, 320, 54
- Noordermeer, E., van der Hulst, J. M., Sancisi, R., Swaters, R. A., & van Albada, T. S. 2005, *A&A*, 442, 137
- Pierini, D., Popescu, C. C., Tuffs, R. J., & Völk, H. J. 2003, *A&A*, 409, 907
- Rand, R. J., Wood, K., Benjamin, R. A., & Meidt, S. E. 2011, *ApJ*, 728, 163
- Rhee, M.-H., & van Albada, T. S. 1996, *A&AS*, 115, 407
- Sanders, D. B., & Mirabel, I. F. 1996, *ARAA*, 34, 749
- Sanders, D. B., et al. 2003, *AJ*, 126, 1607
- Seaquist, E., Yao, L., Dunne, L., & Cameron, H. 2004, *MNRAS*, 349, 1428
- Sofue, Y. 1987, *PASJ*, 39, 547
- Solomon, P. M., & Sage, L. J. 1988, *ApJ*, 334, 613
- Stevens, J. A., & Gear, W. K. 2000, *MNRAS*, 312, L5
- Swarup, G. 1991, *Current Science*, 60, 106
- Swarup, G., et al. 1991, *Current Science*, 60, 95
- Tabatabaei, F. S., Beck, R., & Berkhuijsen, E. 2010a, *Highlights of Astronomy*, Vol. 15, p. 417
- Tabatabaei, F. S., & Berkhuijsen, E. 2010b, *A&A*, 517, 77
- Thompson, T. A., Quataert, E., & Murray, N. 2009, *MNRAS*, 397, 1410
- Tielens, A. G. G. M. 2006, *The Physics and Chemistry of the Interstellar Medium*, Cambridge University Press, Cambridge
- Troland, T. H., & Heiles, C. 1986, *ApJ*, 301, 339
- Tüllmann, R., & Dettmar, R.-J. 2000, *A&A*, 362, 119
- Tüllmann, R., et al. 2006, *A&A*, 448, 43
- Tully, R. B. 1988, *Nearby Galaxies Catalog*, (Cambridge University Press, Cambridge)
- Tully, R. B., et al. 1996, *AJ*, 112, 2471
- Verheijen, M. A. W., & Sancisi, R. 2001, *A&A*, 370, 765
- Vinyaikin, E. N. 2007, *ARep*, 51, 87
- Vlahakis, C., Dunne, L., & Eales, S. 2005, *MNRAS*, 364, 1253
- Wang, Q. D., et al. 1995, *ApJ*, 439, 176
- Wang, Q., et al. 2001, *ApJ*, 555, L99
- Whaley, C. H., Irwin, J. A., Madden, S. C., Galliano, F., & Bendo, G. J. 2009, *MNRAS*, 395, 97
- Willmer, C. N. A., et al. 2009, *AJ*, 138, 146
- Wright, E. L. et al. 2010, *AJ*, 140, 1868
- Wunderlich, E., & Klein, U. 1988, *A&A*, 206, 47
- Young, J. S., et al. 1995, *ApJS*, 98, 219
- Young, J. S., et al. 1996, *AJ*, 112, 1903
- Yun, M. S., Reddy, N. A., & Condon, J. J. 2001, *ApJ*, 554, 803
- Zhu, M., Gao, Y., Seaquist, E. R., & Dunne, L. 2007, *AJ*, 134, 118

This figure "colour_fig.jpg" is available in "jpg" format from:

<http://arxiv.org/ps/1306.0226v1>